Constant-head step injection tests to quantify the stress dependence of fracture transmissivity in an excavation damaged zone: A case study from the Horonobe Underground Research Laboratory

Eiichi Ishii

Horonobe Underground Research Center, Japan Atomic Energy Agency, Horonobe-cho, Japan

A B S T R A C T

In an underground repository for high-level radioactive waste disposal, fracture transmissivity in an excavation damaged zone (EDZ) along tunnels or deposition holes can decrease during the post-closure period via processes such as self-sealing by clay-swelling at the EDZ's fracture surface or an increase in effective normal stress acting on the fractures owing to swelling of backfilling or buffer materials. Hydromechanical coupling models for the stress-dependence of fracture transmissivity are helpful to estimate the change in an EDZ's fracture transmissivity after closure. The applicability of the applied models should be confirmed by in situ tests at the given site; this appears to be facilitated by using constant-head step injection tests. However, injection testing is rarely applied to EDZ fractures. To investigate the applicability of injection tests, the present study performed them on single, tensile EDZ fractures in the Horonobe Underground Research Laboratory hosted by poorly swelling mudstone. Furthermore, the Barton–Bandis normal stress-dependent fracture-closure model quantified the stress-dependence of EDZ facture transmissivity. The fracture's hydraulic aperture increased gradually during injection, and its variation was well reproduced by fitting the model. Although the model requires the normal stress, this parameter was reasonably estimated by the fitting analyses. Constant-head step injection tests coupled with the Barton–Bandis model is believed to be a convenient method for preliminarily quantifying or verifying the stress dependence of EDZ fracture transmissivity, at least for poorly self-sealed, tensile EDZ-fractures.

1. Introduction

In an underground repository for high-level radioactive waste disposal, any excavation damaged zone (EDZ) along tunnels or deposition holes can be a pathway for radionuclides, which may leak into groundwater from waste during the post-closure period. The EDZs can also act as efficient escape channels for any gases produced from the degradation of repository engineering materials during the post-closure period. Therefore, the long-term permeability of any EDZ must be considered when designing a repository and assessing its safety.[1] The permeability of EDZs in underground research laboratories built in mudstone has been reported to be several orders of magnitude higher than that of the host rock. However, an EDZ's permeability can be reduced by self-sealing its fractures via clay swelling at the fracture surfaces owing to re-saturation of the EDZ or by increasing the effective stress generated by swelling of buffer or backfilling materials.[2–4] Not limited to mudstone, the permeability of EDZs may also change by variation of effective stress resulting from the thermal effects of waste,

uplift and denudation, and glaciation.[5–10] Thus, assessment of the long-term permeability of an EDZ needs to consider such changes occurring post-closure.

Numerous in situ experiments to understand changes in the permeability of an EDZ in mudstone have been performed at underground research laboratories. At the Mont Terri rock laboratory (Switzerland) and the Meuse/Haute Marne site (France)—which are both hosted in mudstone with a high capacity for swelling—in situ experiments investigated changes in permeability of re-saturated EDZs over a period of years; they confirmed that hydraulic conductivity/transmissivity eventually reduced by 2–4 orders of magnitude.[11–13] This reduction in permeability has been attributed to swelling of smectite at the EDZ's fracture surface related to matric suction or osmotic suction.[13,14] Changes in EDZs' permeability due to stress variation have also been investigated by in situ plate-loading experiments: loading up to 5 MPa against the tunnel wall from the inside has been reported to reduce the EDZ's fracture transmissivity by 2 orders of magnitude at Mont Terri, and loading up to 4 MPa reduced the transmissivity by 1–4 orders of
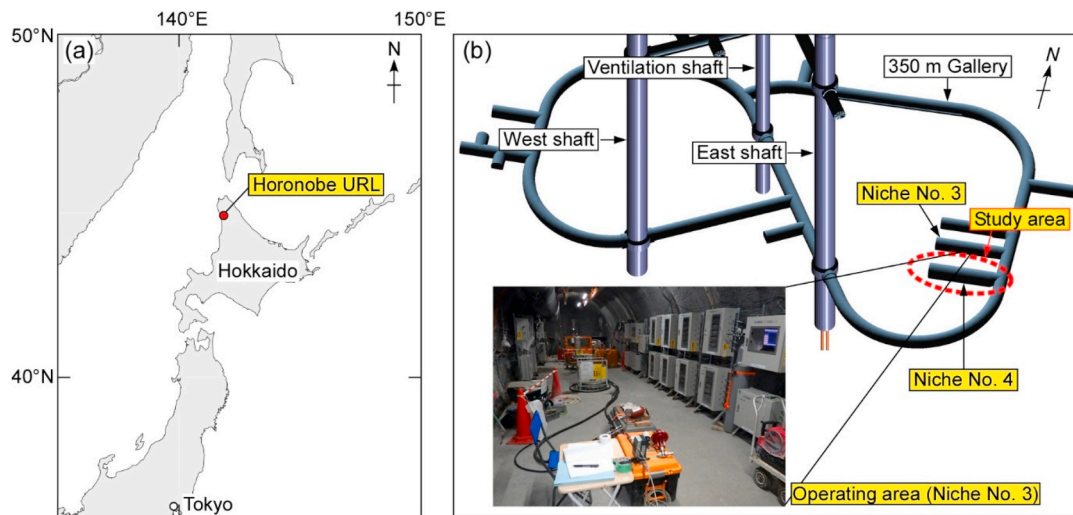
Fig. 1. Locations of (a) the Horonobe URL and (b) the study area (Niche No. 4) and operating area (Niche No. 3) at 350 m below ground level in the URL.

Table 1
Properties of the host rock[30–35].

Property	Value
Mineralogy (wt.%)	
Silica (mainly opal–CT)	40–50
Clay	19–33
Smectite	10–18
Quartz	9–13
Feldspar	7–13
Unconfined compressive strength (MPa)	15.4 ($\pm$2.59)
Indirect tensile strength (MPa)	1.83 ($\pm$0.37)
Young's modulus (GPa)	1.82 ($\pm$0.38)
Poisson's ratio	0.17 ($\pm$0.07)
Swelling pressure index (MPa)[a]	<0.04
Swelling strain index (%)[b]	<0.2
Effective porosity (%)	41.6 ($\pm$0.54)
Skempton's coefficient, B	0.82–0.93
Effective stress coefficient, α	0.80–1.05
Intrinsic permeability (m^2)	$\leq 10^{-18}$

[a] Swelling pressure under conditions of zero volume change.[36]
[b] Swelling strain for a radially confined specimen with axial surcharge.[36]

magnitude at Meuse/Haute Marne.[13,15] Changes in EDZ permeability due stress variation have been further investigated at Mont Terri using a micro tunnel (diameter = 1 m; length = 13 m) with a mega-packer system installed inside: the packer applied pressure up to 2 MPa, which reduced the EDZ permeability by 1–2 orders of magnitude.[16,17] These loading experiments are very useful for confirming the stress dependence of fractures' transmissivity. However, they require large, specialized loading equipment, and are not easily conducted.

Hydromechanical coupling models for quantifying the stress dependence of fracture transmissivity in EDZs have been proposed; these can help estimate changes in the permeability of an EDZ.[17,18] However, before adopting any model, its applicability must be confirmed by in situ experiments at the given site. Constant-head step injection testing is an effective in situ test method for confirming the stress dependence of fracture transmissivity on the field scale; it can be feasibly conducted using a conventional packer system without large-scale, specialized equipment such as a plate-loading system or mega-packer.[19–21] Constant-head step injection testing may also be helpful for quantifying or verifying the stress dependence of fracture transmissivity on the field scale. Nevertheless, although case studies
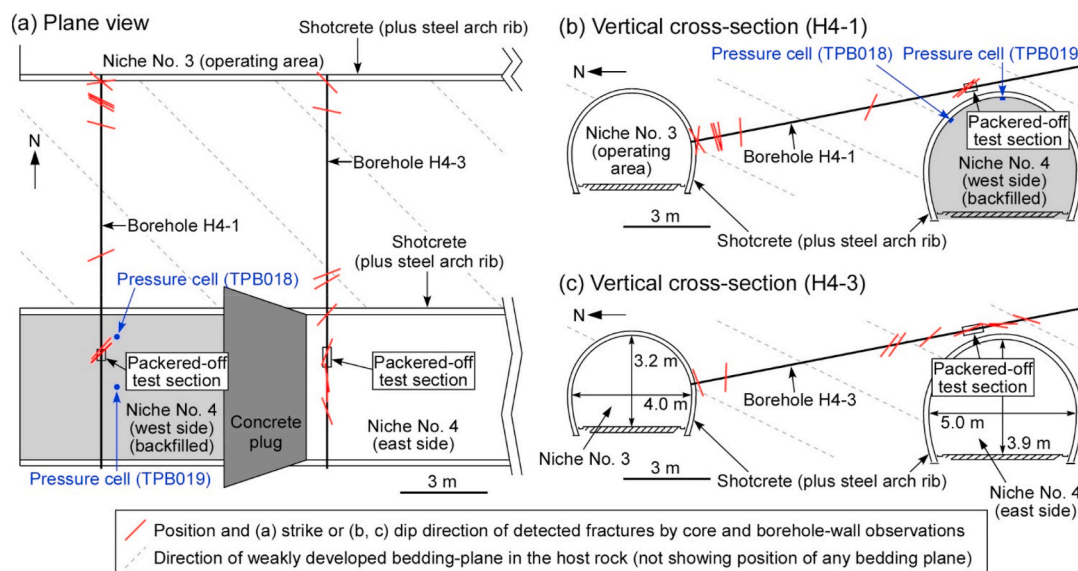

Fig. 2. Layout of boreholes H4-1 and H4-3 drilled from Niche No. 3 and the packered-off test sections (a: plan view; b and c: cross-section). Positions and directions of EDZ fractures detected by core logging and borehole-wall imaging are derived from previous investigations.[37]
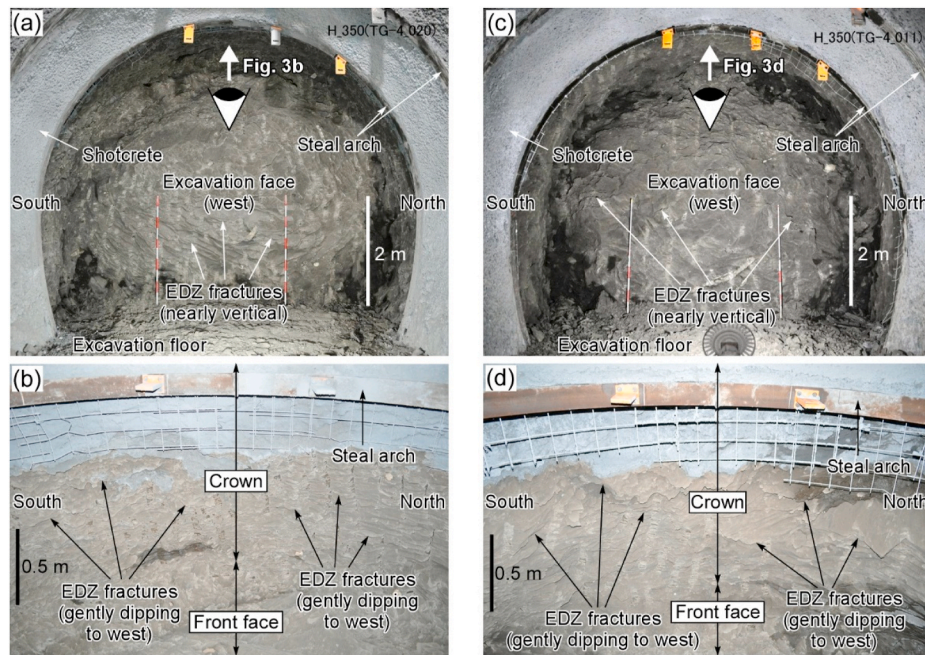
Fig. 3. Photographs of excavation faces during tunneling for Niche No. 4 at locations immediately below boreholes (a, b) H4-1 and (c, d) H4-3. Numerous EDZ fractures with trace lengths of dozens of centimeters are visible on the excavation faces.

have reported constant-head step injection testing in an EDZ,[22] reports of using injection tests to quantify or verify the stress dependence of EDZs' fracture transmissivity are scarce.

To investigate the applicability of constant-head step injection tests for quantifying or verifying the stress dependence of EDZs' fracture transmissivity on the field scale, the present work reports injection testing of single EDZ fractures in siliceous mudstone at the Horonobe Underground Research Laboratory (URL; Fig. 1a) and verification of the applicability of the Barton–Bandis normal stress-dependent fracture-closure model[23,24] as a case study. The siliceous mudstone includes smectite, but consists mainly of a large amount of opal–cristobalite/-tridymite (opal–CT). Its swelling capacity is therefore very poor; i.e., the swelling pressure index is <0.04 MPa, and the swelling strain index is <0.2% (Table 1), whereas those parameters for mudstone capable of swelling well are typically ≥1 MPa and ≥1%, respectively.[3] Siliceous mudstone is thus advantageous in that the effect of self-sealing by clay swelling is ruled out when evaluating any change in EDZ fracture transmissivity, so the stress dependence of fracture transmissivity can be evaluated more directly. The Barton–Bandis model is adopted here for the following reasons. (1) It is a widely known hydromechanical coupling model for fracture transmissivity.[25–28] (2) It is applicable if three easily measurable parameters are available: the hydraulic aperture of the fracture; the joint coefficient roughness (JRC_0) on the laboratory scale (~0.1 m in length) for the fracture surface; and the tensile strength of the intact rock.[29]

2. Geological setting

Constant-head step injection tests were performed on two single fractures in an EDZ formed along Niche No. 4 at 350 m below ground level in the Horonobe URL (Fig. 1b). The host rock is a Neogene siliceous mudstone of the Wakkanai Formation. Table 1 lists its properties. Two boreholes (H4-1 and H4-3; drilling length, 14.0 m; diameter, 0.1 m) were drilled from Niche No. 3 (Fig. 1b) to the EDZ that formed above the crown of Niche No. 4 after its excavation (Fig. 2). These niches are EW-extending and horizontal tunnels, which were mechanically excavated toward west using a breaker in horizontal steps of 1.0 m (Fig. 3). After each step, 0.2 m-thick shotcrete and a steel arch rib were installed (Figs. 2 and 3). The maximum inner diameter is 4.0 m for Niche No. 3 and 5.0 m for Niche No. 4 (Fig. 2c). Observations of the boreholes' cores and walls confirmed the positions and directions of fractures in the boreholes,[37] which depend on the structure of the tunnels (Fig. 2); i.e., fracture strikes are nearly parallel to the tunnel axis near the tunnel sidewall and nearly normal to the tunnel axis near the crown (Fig. 2a), while the fractures' dip directions are nearly parallel to the tunnel wall/crown (Fig. 2b and c). The fracture surfaces exhibit plumose structures indicating tensile failure.[37] Furthermore, a previous borehole investigation prior to the tunnel excavation confirmed the occurrence of few natural fractures in the study area,[38] and fractures were only observed in the two boreholes near the tunnel (Fig. 2). Thus, the fractures can be interpreted as EDZ fractures.[30,39] Although fractures are also observed 1.6 m from Niche No. 3 and 2.3 m from Niche No. 4
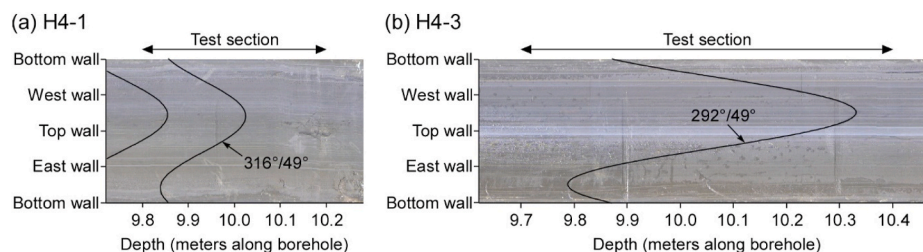

Fig. 4. Borehole-wall images for each test section and sine curves (solid lines) fitted to the fractures.[37]
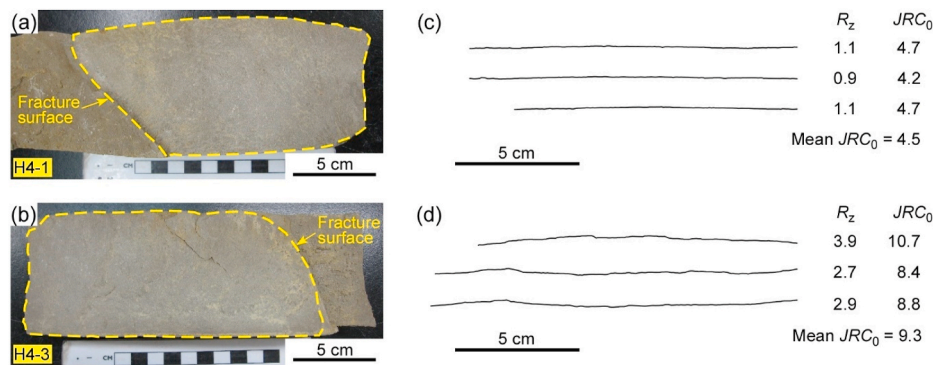
Fig. 5. Fracture surfaces on drill cores of tested fractures for boreholes (a) H4-1 and (b) H4-3. Trace profiles on the fracture surfaces, measured R_z, and calculated JRC_0 for boreholes (c) H4-1 and (d) H4-3. R_z is maximum height of fracture-surface profile (mm), and JRC_0 is joint roughness coefficient at laboratory scale.
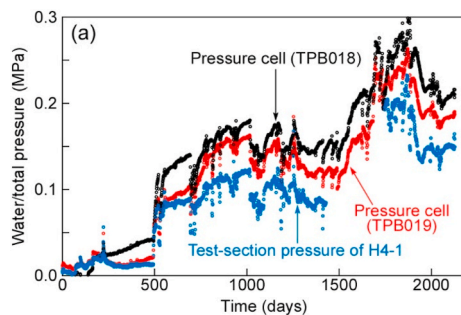

Fig. 6. Test-section pressure of borehole H4-1 and total pressures monitored by pressure cells installed near the crown of Niche No. 4 (TPB018 and TPB019 in Fig. 2a and b) during from the contact-sealing around the plug to the injection test.

(Fig. 2)—these can be regarded as fractures in the outer part of the EDZ[40]—the extent of the EDZ in which fractures are well developed (i.e., the inner part of the EDZ[40]) is typically limited to ≤0.6 m from the tunnel wall in the study area.[30] Mechanical aperture of EDZ fractures were also observed by in situ resin-injection testing around Niche No. 3; the mechanical aperture was 0.08–0.31 mm within 0.2 m of the tunnel's excavation wall and 0.03–0.13 mm at 0.4–0.7 m from the tunnel's excavation wall, which decreased with distance from the tunnel's excavation wall.[41] Geological wall-mapping during tunnel excavations of Niche No. 4 confirmed numerous EDZ fractures on the excavation wall (Fig. 3). Surface-based borehole investigations established the initial principal stress conditions in the study area prior to construction of the URL as being 7.6 MPa for the EW direction (horizontal), 5.5 MPa for the NS direction (horizontal), and 5.6 MPa vertically.[30]

Packered-off test sections were set at the two single EDZ fractures: one 9.95 m along borehole (mabh) H4-1 and the other 9.92 mabh H4-3 (the test sections were 9.8–10.2 mabh H4-1 and 9.7–10.4 mabh H4-3; Fig. 2). The directions of fracture (given as dip direction/dip angle) are 316°/49° for H4-1 and 292°/49° for H4-3 (Fig. 4), which are oblique to the direction (225°/35°) of bedding planes that are weakly developed in the host rock (Fig. 2). The JRC_0 required to adopt the Barton–Bandis model is ~4.5 for H4-1 and ~9.3 for H4-3 (Fig. 5). This was computed by the following empirical relationship[42] using the maximum height of the fracture surface profile (R_z, mm; equal to the vertical distance between the highest peak and the lowest valley in the profile) measured with a profile gauge:

$$JRC_0 = 4.4192 R_z^{0.6482}. \tag{1}$$

Although numerous methods for determining JRC_0 have been proposed, that using R_z is simple, practical, and insensitive to the problem of the sampling interval of data points.[42]

The test sections in boreholes H4-1 and H4-3 are both located ~0.4 m from the shotcrete (thickness, 0.2 m) of the crown in Niche No. 4, but their hydromechanical test conditions differ. The west side of Niche No. 4 has been backfilled with 60% rock and 40% bentonite, and closed with a concrete plug (thickness, 3 m; Fig. 2). In situ groundwater (saline water) collected from other locations was supplied into the backfilled tunnel and surrounding EDZ. The water pressure in the test section (called "the test-section pressure") in H4-1 increased gradually from 0 MPa after contact-sealing around the plug and the groundwater supply, and total pressures monitored by two pressure cells[43] installed near the crown in Niche No. 4 (TPB018 and TPB019 in Fig. 2a and b) also increased accordingly (Fig. 6). The total pressure in the pressure cells increased owing to increasing water pressure within the tunnel and the swelling pressure of backfilling materials. Abrupt changes in water/total pressures shown in Fig. 6 are attributed to changes in the flow rate of the groundwater supply into the tunnel and surrounding EDZ. The test-section pressure of H4-1 immediately before the injection test was ~0.15 MPa; the test section and surrounding area are thought to have been saturated, although previous investigations[37,44] have indicated that the test section may contain gases (CH_4 and CO_2)[45] degassed from the groundwater. In borehole H4-3, the east side of Niche No. 4 has not been backfilled, thus the test-section pressure here was almost 0 MPa.[37,44]

3. Method

3.1. Injection testing

Two constant-head step injection tests were performed to the single fracture in each test-section of boreholes H4-1 and H4-3 (Fig. 2). The tests employed multi packer systems previously installed in the boreholes. A plunger pump (12 L min^{-1} maximum injection flow rate) and accumulator tank were used for injection, and poly-ether-ether-ketone (PEEK) tubes (inner diameter 6–8 mm), stainless-steel rods (inner diameter 10 mm), and pressure-resistance hose (inner diameter 25 mm) were used as an injection line into each test section. The test-section pressure was increased in steps of ~0.1 MPa; it was manually controlled by adjusting the injection flow rate with a releasing valve installed on the downstream side of the pump. The injection flow rate was monitored by a mass flow meter (maximum measurable flow rate, 10 L min^{-1}), and the test-section pressure was monitored by a pressure sensor installed in the operating area (Niche No. 3 in Fig. 1b); connections were by PEEK tubes. Water injection was continued at a constant head for 5 or 10 min during each step (10 min for the first test and 5 min for the second). The water pressures in the upper and lower packers of the test section were maintained at 4.6 MPa through continuous pressurization with nitrogen gas. The recording interval was 1 s.
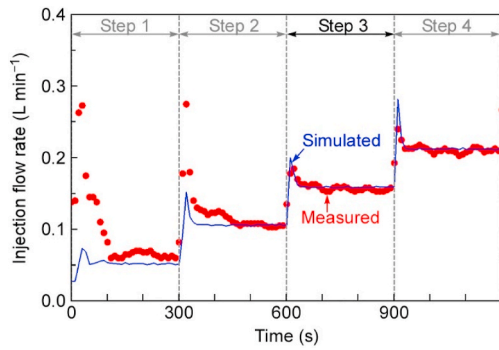
Fig. 7. Representative fitting analysis between measured and simulated flow rates for each injection step. Step 3 during the second test for borehole H4-1 is the given example.
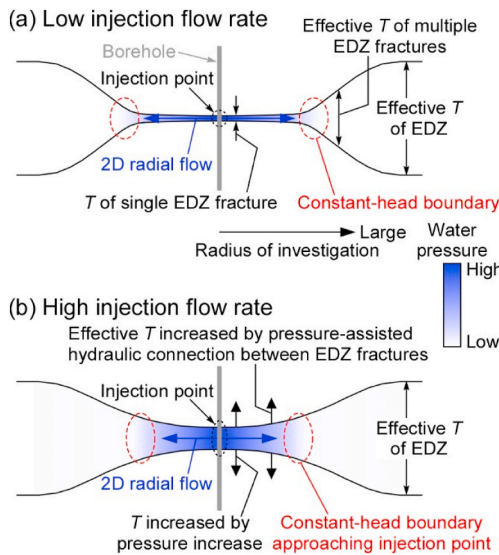

Fig. 8. Schematic model showing changes of transmissivity (T) of the assumed aquifer and its outer region with increasing radius of investigation during injection testing. The extent of the assumed aquifer is from the injection point to the constant-head boundary.

3.2. Estimation of fracture transmissivity and hydraulic aperture during injection testing

To estimate the transmissivity of the single fracture in each test section during injection testing, the test-section pressure and injection flow rate were analyzed using well test analysis software (nSIGHTS, n-dimensional Statistical Inverse Graphical Hydraulic Test Simulator[46,47]). This program simulates a single-phase, radial/non-radial flow regime with a borehole at the center of the modeled flow system. The present study determined the transmissivity of the single fracture during each injection step by fitting the measured and simulated flow rates, while the simulation considered entire injection steps as the pressure history (Fig. 7), similar to previous studies.[21] Each single fracture was modeled as a homogeneous, horizontal, and finite aquifer with the same thickness as the test section (i.e., 0.4 m for H4-1 and 0.7 m for H4-3) and surrounded by a constant-head boundary, where a radial laminar flow was assumed. This boundary condition is based on the assumption that the tested EDZ fractures link hydraulically to numerous other EDZ fractures (as observed on the excavation faces in Fig. 3), which may together behave as a significantly more permeable zone than the tested "single" EDZ fractures; thus the tested single fractures can be considered to be hydraulically surrounded by a constant-head boundary (Fig. 8a).

Assuming the tested fractures are disk-shaped, their radii are inferred to be dozens of centimeters from geological wall-mapping during tunnel excavation (Fig. 3). The static formation pressure was the same as the test-section pressure immediately before injection for each test section. The compressibility of each test section within the borehole was 5×10^{-8} Pa^{-1} based on results from previous pulse tests[37,44] and thus apparently higher than those of water and the packers, indicating that the test sections contained gases (CH_4 and CO_2) that were degassed from the groundwater, as reported previously.[37,44] The fitting parameters were the transmissivity, storativity, and radius of the assumed aquifer. During fitting analysis, 50 simulations were performed for each injection step, and the geometric mean value of the simulated transmissivity, and the geometric mean value of storativity, and the arithmetic mean value of the simulated radius were determined as the transmissivity, storativity, and radius of the assumed aquifer during each injection step. Finally, the hydraulic aperture e (m) (a theoretical smooth wall aperture) of the tested EDZ fractures was derived from the estimated transmissivity based on the parallel-plate model[48]:

$$T = ge^3/12\nu \tag{2}$$

where T is the transmissivity of a fracture (m^2 s^{-1}); g is the acceleration due to gravity (9.806 m s^{-2}); and ν is the kinematic viscosity of the fluid (1.0×10^{-6} m^2 s^{-1} for pure water at 20 °C). In addition, $(1/T_1) \times (dT/dh)$ (m^{-1}) was also calculated from the estimated T to further characterize the stress dependence of fracture transmissivity,[49] where T_1 is the baseline transmissivity (m^2 s^{-1}) and h is the hydraulic head (m).

Furthermore, to check the validity of the assumption that T is distributed homogeneously in the tested EDZ fractures, the flow dimension[50] in the tested fractures during each injection step was also investigated by the fitting analysis. An estimated flow dimension close to 2.0 (i.e., two-dimensional radial flow) would indicate the transmissivity distribution in the tested EDZ fractures to be homogeneous under the applied conditions; i.e., the fracture transmissivity is scale-independent. The possibility of scale dependence under certain conditions is an important consideration when applying laboratory-scale data to field-scale modeling.[51] If the simulated flow dimension in the tested EDZ fractures is close to 2.0, then the Barton–Bandis model based on laboratory-scale tests will be applicable to evaluate the stress dependence of the EDZ's fracture transmissivity. More-precise checking of the homogeneity of the transmissivity distribution requires a fully coupled model, as proposed by Murdoch and Germanovich.[52]

3.3. Application of the Barton–Bandis model

To apply the Barton–Bandis model to the variation in hydraulic aperture of the tested fractures during injection, fitting analyses were performed here and the coefficients of determination (r^2) were calculated. The Barton–Bandis normal stress-dependent fracture-closure model is expressed as follows[23,24]:

$$e = JRC_0^{2.5} / (E/e)^2 \, (e \text{ and } E; \text{ in microns}) \tag{3}$$

$$E = E_0 - (1/V_m + K_{ni}/\sigma'_n)^{-1} \tag{4}$$

$$E_0 = V_m + E_r \tag{5}$$

where E is the mechanical aperture of a fracture (mm); E_0 is the initial mechanical aperture (mm) under self-weight stress (~1 kPa); V_m is the maximum closure (mm); K_{ni} is the initial normal stiffness (MPa mm^{-1}); σ'_n is the effective normal stress (MPa); and E_r is the residual aperture (mm). Note that the units of e and E in Eq. (3) are microns.

Eq. (3) is only valid for $E \geq e$ and when shear displacement is small and gouge production is negligible.[24,53] If it results in $E < e$, the E and e are assumed to be equal.[23] This equation relates E and e, even at the field scale, as it is unlikely that fracture closure is size-dependent, unlike
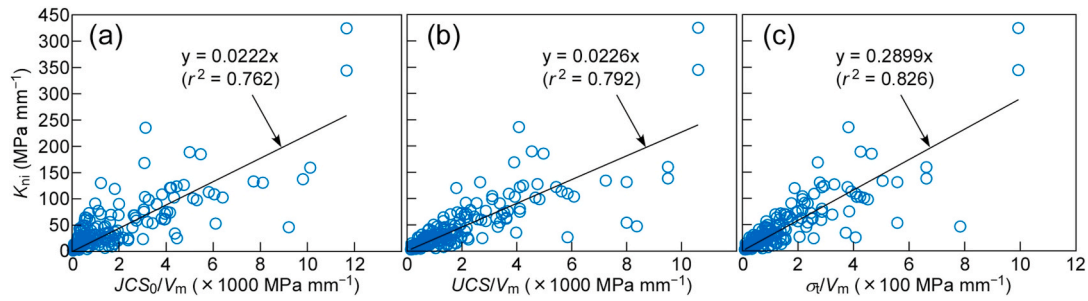
Fig. 9. K_{ni} versus (a) JCS_0/V_m, (b) UCS/V_m, and (c) σ_t/V_m,[29] based on the laboratory-experimental data of Bandis[64] for a variety of natural fractures and rocks. JCS_0 is joint wall compressive strength at laboratory scale (MPa), K_{ni} is initial normal stiffness of fracture (MPa mm^{-1}), V_m is maximum closure of fracture (mm), UCS is unconfined compressive strength of intact rock (MPa), and σ_t is indirect tensile strength of intact rock (MPa).
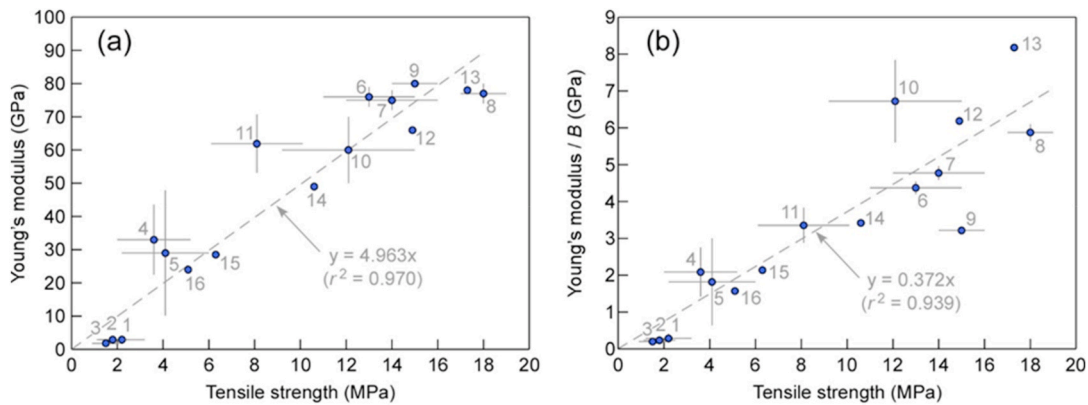

Fig. 10. (a) Young's modulus and (b) Young's modulus/B versus indirect tensile strength of various intact rocks, and the approximation lines,[29] where B is unconfined compressive strength (MPa)/indirect tensile strength (MPa). 1–3: siliceous mudstone, 4–5: marl, 6–9: granite/granodiorite, 10: gneiss, 11: granite/gneiss, 12: slate, 13: dolerite, 14: limestone, 15: siltstone, and 16: sandstone.

shear strength–displacement behavior.[23,54,55] The equation is approximate,[56] but is widely used to convert measured e to E or simulated E to e at field scale in a variety of geoengineering problems.[57–61] Nevertheless, Eq. (3) is validly applicable at the field scale when the fracture transmissivity can be assumed to be homogeneous and scale-independent (i.e., the flow dimension in the fractures is close to 2.0). Conversely, it may be invalidated by significant scale dependence.

The following equations are applicable for the values of E_0 and K_{ni}^{29}:

$$E_0 \approx V_m \ (\text{or } E_r \approx 0) \tag{6}$$

$$K_{ni} = 0.2899\sigma_t/V_m \ \left(r^2 = 0.826\right) \tag{7}$$

where σ_t is the indirect tensile strength of the intact rock (MPa), which can be determined from laboratory tests.[62] Eq. (7) was empirically derived using the laboratory-experimental data of Bandis et al.[63] for natural fractures in a variety of rocks including of limestone, sandstone, siltstone, slate, and dolerite, and Eq. (7) showed the best fit among some relationships[29] (Fig. 9). This equation is reasonable, considering that the indirect σ_t of intact rocks correlated well with Young's modulus[29] (Fig. 10). Integrating Eqs (4), (6) and (7) leads to the following equation[29]:

$$E_0 = E\left(1 + \sigma_n^{'}/0.2899\sigma_t\right). \tag{8}$$

The value of σ'_n for a fracture is given as follows:

$$\sigma_n^{'} = \sigma_n - \alpha p \tag{9}$$

where σ_n is the total normal stress (MPa); α is the effective stress coefficient (or Biot's coefficient[65]); and p is the water pressure (MPa).

Although α is usually assumed to be 1 for a fracture,[66–68] it may be much lower for a rough fracture, depending on the σ_n, particularly when the intact rock behaves as impermeable.[69] The value of α for a fracture should be greater than (or equal to) that for the intact rock if the host rock is regarded as permeable/porous.[70] The host rock studied here has very low permeability (Table 1), and was thus effectively impermeable during injection testing, given the very short test time. For an impermeable host rock, the value of α for a rough fracture can be expressed as follows[69]:

$$\alpha = \left(1 + (\sigma_n - p)/K_{ni}V_m\right)^{-1} \ (\sigma_n \geq p) \tag{10}$$

$$\alpha = 1 \ (\sigma_n < p). \tag{11}$$

Eq. (10) can be modified to the following equation by integrating Eq. (7):

$$\alpha = \left(1 + (\sigma_n - p)/0.2899\sigma_t\right)^{-1}. \tag{12}$$

Thus, the value of σ'_n for the fractures during injection testing is given as follows:

$$\sigma_n^{'} = \sigma_n - p_0 - (p - p_0)\left/\left(1 + (\sigma_n - p)/0.2899\sigma_t\right)\right. \tag{13}$$

where p_0 is the initial water pressure immediately before injection.

The unknown parameters σ_n and E_0 were determined here by fitting values of e estimated by the flow simulation and calculated using least squares from the hydromechanical model expressed by Eqs (3), (8) and (13). The inputted value of JRC_0 was 4.5, 4.2, and 4.7 for H4-1 and 9.3, 8.4, and 10.7 for H4-3 (i.e., the mean, minimum, and maximum values shown in Fig. 5, respectively); σ_t was 1.83, 1.46, and 2.21 MPa (i.e., the mean, and its $+1\sigma$ and -1σ values, as shown in Table 1); p was the test-section pressure; and p_0 was 0.152 and 0.153 MPa for the first and
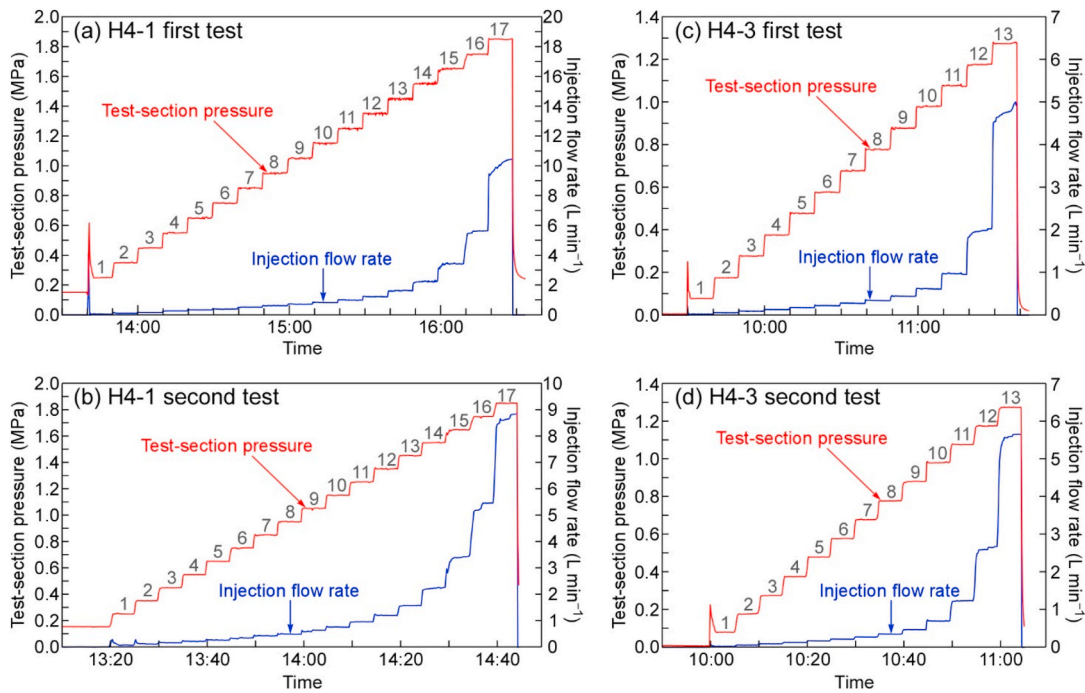
Fig. 11. Test-section pressure and injection flow rate during the first and second tests for borehole (a, b) H4-1 and (c, d) H4-3. The steps in the constant-head step injection tests are numbered. Data are available in Supplementary Material.
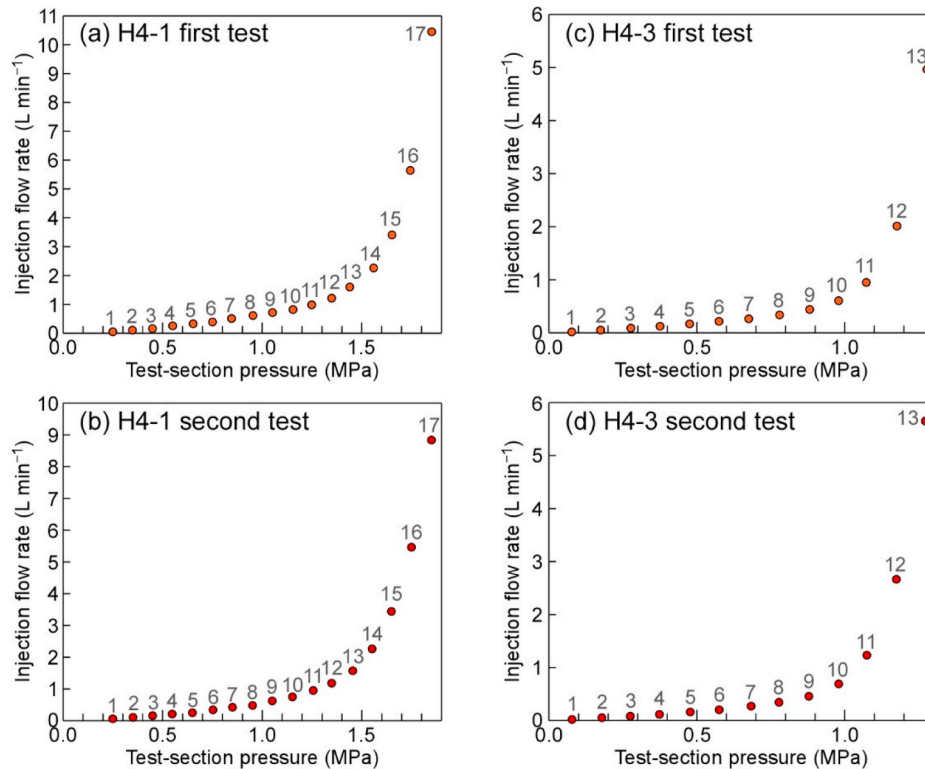
Fig. 12. Injection flow rate vs test-section pressure at the end of each injection step during the first and second tests for borehole (a, b) H4-1 and (c, d) H4-3. Each point is labeled with the step number.

second tests in H4-1 and 0 MPa for all tests in H4-3.

The normal stiffness of the fractures during injection testing was also calculated from the simulated σ_n and E_0. The normal stiffness can be converted to the storativity of the fractures,[71] which can then be compared with the storativity estimated by the flow simulation to verify

the validity of the simulated values of σ_n, E_0, and other parameters. The normal stiffness K_n (MPa mm^{-1}) of a fracture can be derived as follows[63]:

$$K_n = K_{ni}\left(1 - \sigma_n'/(V_m K_{ni} + \sigma_n')\right)^{-2}. \tag{14}$$
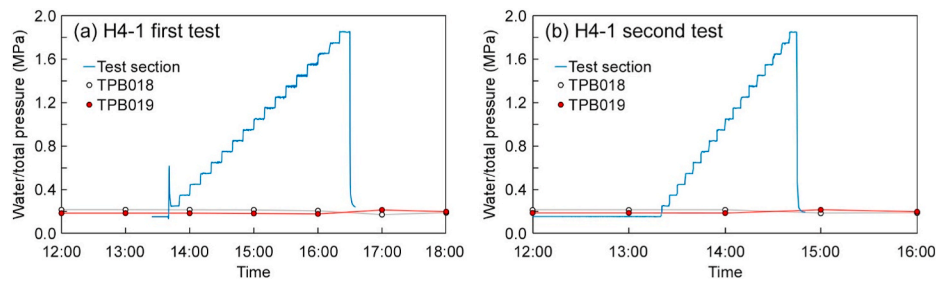
Fig. 13. Test-section pressure of borehole H4-1 and total pressures monitored by pressure cells installed near the crown of Niche No. 4 (TPB018 and TPB019 in Fig. 2a and b) during the first and second tests.

Table 2
Injection flow rate q (L min^{-1}) and test-section pressure p (MPa) measured at the end of each injection step, transmissivity T (m^2 s^{-1}), storativity S (−), radius r (m), hydraulic aperture e (mm), and $(1/T_1) \times (dT/dh)$ ($\equiv M$, $\times 10^{-2}$ m^{-1}; T_1 is baseline T, and h is hydraulic head (m)) estimated by flow simulation, and mechanical aperture E (mm), effective stress coefficient α (−), effective normal stress σ'_n (MPa), fracture normal stiffness K_n (MPa mm^{-1}), and S estimated by the hydromechanical model (Eq. (3), (8), and (13)) when given the mean values for JRC_0 and σ_t for each injection step in H4-1.

Step no.	Measurement		Flow simulation					Hydromechanical model				
	q	p	T	S	r	e	M	E	α	σ'_n	K_n	S
H4-1 first test												
1[a]	0.045	0.250	1.40×10^{-7}	3.06×10^{-6}	0.63	–	–	–	–	–	–	–
2[a]	0.098	0.348	3.14×10^{-8}	1.18×10^{-6}	0.55	–	–	–	–	–	–	–
3[a]	0.158	0.449	3.25×10^{-8}	1.74×10^{-7}	0.53	–	–	–	–	–	–	–
4	0.255	0.550	4.15×10^{-8}	2.09×10^{-8}	0.61	0.037	–	0.038	0.26	1.80	61.91	4.12×10^{-8}
5	0.323	0.653	4.16×10^{-8}	2.33×10^{-8}	0.59	0.037	0.01	0.038	0.27	1.77	60.14	4.46×10^{-8}
6	0.385	0.751	4.08×10^{-8}	3.99×10^{-8}	0.60	0.037	−0.09	0.039	0.29	1.74	58.29	4.85×10^{-8}
7	0.508	0.846	4.55×10^{-8}	6.32×10^{-8}	0.56	0.038	0.31	0.040	0.30	1.70	56.34	5.29×10^{-8}
8	0.610	0.954	4.74×10^{-8}	2.00×10^{-8}	0.56	0.039	0.34	0.040	0.32	1.65	53.89	5.90×10^{-8}
9	0.715	1.052	4.85×10^{-8}	9.16×10^{-8}	0.54	0.039	0.33	0.041	0.34	1.60	51.43	6.57×10^{-8}
10	0.815	1.155	4.98×10^{-8}	8.24×10^{-7}	0.53	0.039	0.32	0.043	0.37	1.54	48.55	7.46×10^{-8}
11	0.980	1.249	5.46×10^{-8}	9.56×10^{-8}	0.53	0.041	0.44	0.044	0.40	1.47	45.63	8.49×10^{-8}
12	1.210	1.349	6.18×10^{-8}	1.10×10^{-7}	0.53	0.042	0.60	0.046	0.43	1.40	42.17	9.93×10^{-8}
13	1.598	1.440	7.38×10^{-8}	1.44×10^{-7}	0.51	0.045	0.86	0.048	0.46	1.31	38.64	1.17×10^{-7}
14	2.260	1.560	9.32×10^{-8}	1.26×10^{-7}	0.50	0.048	1.21	0.051	0.51	1.18	33.35	1.51×10^{-7}
15	3.405	1.652	1.30×10^{-7}	2.15×10^{-7}	0.47	0.054	1.90	0.055	0.57	1.06	28.73	1.93×10^{-7}
16	5.638	1.744	1.94×10^{-7}	2.18×10^{-7}	0.46	0.062	3.01	0.061	0.63	0.91	23.57	2.61×10^{-7}
17	10.448	1.852	3.28×10^{-7}	2.36×10^{-7}	0.45	0.074	5.20	0.072	0.72	0.69	16.83	4.18×10^{-7}
H4-1 second test												
1[a]	0.060	0.249	5.62×10^{-8}	6.44×10^{-6}	0.67	–	–	–	–	–	–	–
2[a]	0.105	0.350	3.59×10^{-8}	2.08×10^{-6}	0.56	–	–	–	–	–	–	–
3	0.158	0.449	3.36×10^{-8}	2.84×10^{-8}	0.59	0.035	–	0.037	0.25	1.84	64.81	3.73×10^{-8}
4	0.210	0.547	3.39×10^{-8}	1.82×10^{-8}	0.60	0.035	0.08	0.037	0.26	1.82	63.24	4.00×10^{-8}
5	0.253	0.649	3.43×10^{-8}	1.50×10^{-8}	0.66	0.035	0.11	0.038	0.27	1.78	61.47	4.33×10^{-8}
6	0.343	0.752	3.52×10^{-8}	6.53×10^{-8}	0.58	0.035	0.15	0.038	0.29	1.75	59.52	4.73×10^{-8}
7	0.423	0.850	3.82×10^{-8}	3.58×10^{-8}	0.60	0.036	0.34	0.039	0.30	1.71	57.48	5.17×10^{-8}
8	0.480	0.951	3.84×10^{-8}	4.35×10^{-8}	0.59	0.036	0.28	0.040	0.32	1.66	55.17	5.71×10^{-8}
9	0.625	1.050	4.23×10^{-8}	3.44×10^{-8}	0.56	0.037	0.43	0.041	0.34	1.61	52.67	6.37×10^{-8}
10	0.750	1.151	4.56×10^{-8}	1.09×10^{-7}	0.52	0.038	0.50	0.042	0.37	1.55	49.83	7.20×10^{-8}
11	0.953	1.255	5.39×10^{-8}	4.69×10^{-8}	0.56	0.040	0.74	0.043	0.39	1.48	46.57	8.30×10^{-8}
12	1.183	1.348	5.97×10^{-8}	1.74×10^{-7}	0.51	0.042	0.85	0.045	0.42	1.41	43.32	9.58×10^{-8}
13	1.573	1.454	7.25×10^{-8}	1.13×10^{-7}	0.52	0.045	1.13	0.047	0.46	1.32	39.15	1.16×10^{-7}
14	2.263	1.551	9.45×10^{-8}	1.44×10^{-7}	0.51	0.049	1.62	0.050	0.51	1.21	34.83	1.42×10^{-7}
15	3.443	1.648	1.29×10^{-7}	2.18×10^{-7}	0.47	0.054	2.32	0.054	0.56	1.08	29.97	1.82×10^{-7}
16	5.463	1.749	1.89×10^{-7}	1.83×10^{-7}	0.47	0.061	3.48	0.060	0.62	0.92	24.27	2.52×10^{-7}
17	8.838	1.849	2.84×10^{-7}	2.27×10^{-7}	0.45	0.070	5.22	0.070	0.71	0.72	17.97	3.85×10^{-7}

[a] Possibly affected by gas left within the tested fractures.

Using the mean value of σ_t (i.e., 1.83 MPa), the value of K_n was determined and converted to the unitless fracture storativity, S[49]:

$$S \approx 10^{-9} \gamma \alpha / K_n \qquad (15)$$

where γ is the unit weight of water (9.8 kN m^{-3}).

4. Results

The test-section pressure and injection flow rate during the first and second injection tests are shown in Fig. 11, and Fig. 12 gives values at the end of each step. The injection flow rate increased gradually to ≥ 8.8 L min^{-1} as the test-section pressure increased to 1.8 MPa for H4-1; it reached ≥ 5.0 L min^{-1} as the test-section pressure increased to 1.3 MPa for H4-3. During the injection steps for H4-1, the total pressures monitored at the pressure cells (TPB018 and TPB019 in Fig. 2a and b) did not vary significantly, unlike the test-section pressure (Fig. 13).

The estimated S was 1.50×10^{-8} to 6.44×10^{-6} for H4-1 (Table 2) and 8.55×10^{-8} to 1.34×10^{-5} for H4-3 (Table 3). However, steps 1–3 of the first test for H4-1, steps 1 and 2 of the second test for H4-1, and step 1 of the first and second tests for H4-3 resulted in S over one order of magnitude higher than those for the other steps (Tables 2 and 3).

Table 3

Injection flow rate q (L min^{-1}) and test-section pressure p (MPa) measured at the end of each injection step, transmissivity T (m^2 s^{-1}), storativity S (−), radius r (m), hydraulic aperture e (mm), and $(1/T_1) \times (dT/dh)$ ($\equiv M$, $\times 10^{-2}$ m^{-1}; T_1 is baseline T, and h is hydraulic head (m)) estimated by flow simulation, and mechanical aperture E (mm), effective stress coefficient α (−), effective normal stress σ'_n (MPa), fracture normal stiffness K_n (MPa mm^{-1}), and S simulated by the hydromechanical model (Eq. (3), (8), and (13)) when given the mean values for JRC_0 and σ_t for each injection step in H4-3.

Step no.	Measurement		Flow simulation					Hydromechanical model				
	q	p	T	S	r	e	M	E	α	σ'_n	K_n	S
H4-3 first test												
1[a]	0.018	0.077	2.89×10^{-8}	4.84×10^{-6}	0.88	–	–	–	0.26	1.58	26.16	9.68×10^{-8}
2	0.053	0.175	1.80×10^{-8}	8.55×10^{-8}	0.70	0.028	–	0.082	0.27	1.55	25.48	1.04×10^{-7}
3	0.090	0.277	1.88×10^{-8}	1.04×10^{-7}	0.65	0.028	0.42	0.083	0.29	1.52	24.71	1.14×10^{-7}
4	0.125	0.376	1.95×10^{-8}	1.36×10^{-7}	0.60	0.029	0.41	0.084	0.30	1.49	23.89	1.24×10^{-7}
5	0.168	0.476	2.28×10^{-8}	1.59×10^{-7}	0.67	0.030	0.86	0.086	0.32	1.45	22.97	1.37×10^{-7}
6	0.218	0.575	2.21×10^{-8}	1.43×10^{-7}	0.61	0.030	0.56	0.088	0.34	1.40	21.97	1.52×10^{-7}
7	0.267	0.676	2.45×10^{-8}	1.93×10^{-7}	0.59	0.031	0.70	0.090	0.36	1.35	20.84	1.72×10^{-7}
8	0.338	0.780	2.63×10^{-8}	1.96×10^{-7}	0.59	0.032	0.75	0.093	0.39	1.29	19.54	1.97×10^{-7}
9	0.443	0.882	3.10×10^{-8}	2.84×10^{-7}	0.58	0.034	1.00	0.097	0.42	1.23	18.10	2.30×10^{-7}
10	0.608	0.980	3.70×10^{-8}	3.51×10^{-7}	0.53	0.036	1.28	0.101	0.46	1.15	16.55	2.73×10^{-7}
11	0.950	1.073	5.50×10^{-8}	3.79×10^{-7}	0.54	0.041	2.24	0.107	0.50	1.06	14.89	3.30×10^{-7}
12	2.015	1.177	9.83×10^{-8}	4.73×10^{-7}	0.52	0.049	4.36	0.115	0.56	0.95	12.79	4.26×10^{-7}
13	4.965	1.278	2.14×10^{-7}	6.24×10^{-7}	0.48	0.064	9.65	0.128	0.62	0.80	10.47	5.83×10^{-7}
H4-3 second test												
1[a]	0.020	0.078	2.37×10^{-8}	1.34×10^{-5}	0.87	–	–	–	0.26	1.53	25.80	1.44×10^{-7}
2	0.055	0.179	1.49×10^{-8}	1.97×10^{-7}	0.58	0.026	–	0.081	0.28	1.50	25.07	1.56×10^{-7}
3	0.085	0.275	1.70×10^{-8}	2.01×10^{-7}	0.63	0.027	1.44	0.082	0.29	1.47	24.32	1.69×10^{-7}
4	0.118	0.374	1.93×10^{-8}	1.86×10^{-7}	0.70	0.029	1.50	0.084	0.31	1.43	23.46	1.86×10^{-7}
5	0.163	0.478	1.97×10^{-8}	1.77×10^{-7}	0.63	0.029	1.06	0.086	0.33	1.39	22.47	2.06×10^{-7}
6	0.205	0.576	2.07×10^{-8}	2.24×10^{-7}	0.60	0.029	0.97	0.088	0.35	1.35	21.43	2.30×10^{-7}
7	0.273	0.684	2.35×10^{-8}	1.98×10^{-7}	0.63	0.031	1.13	0.090	0.38	1.29	20.16	2.64×10^{-7}
8	0.345	0.778	2.50×10^{-8}	2.47×10^{-7}	0.59	0.031	1.11	0.093	0.41	1.23	18.91	3.01×10^{-7}
9	0.458	0.879	3.01×10^{-8}	3.48×10^{-7}	0.57	0.033	1.43	0.097	0.44	1.16	17.42	3.55×10^{-7}
10	0.693	0.980	4.03×10^{-8}	2.95×10^{-7}	0.55	0.037	2.09	0.102	0.48	1.08	15.72	4.29×10^{-7}
11	1.233	1.075	6.94×10^{-8}	5.46×10^{-7}	0.58	0.044	4.00	0.109	0.53	0.98	13.93	5.30×10^{-7}
12	2.668	1.175	1.31×10^{-7}	9.68×10^{-7}	0.54	0.054	7.70	0.118	0.59	0.86	11.78	6.96×10^{-7}
13	5.653	1.273	2.48×10^{-7}	1.21×10^{-6}	0.47	0.067	14.01	0.132	0.66	0.71	9.41	9.77×10^{-7}

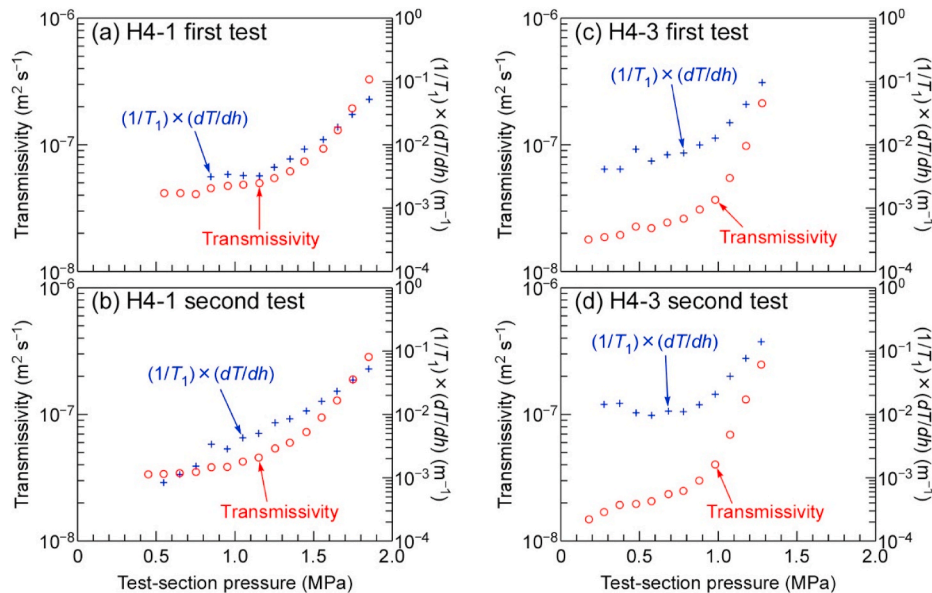[a] Possibly affected by gas left within the tested fractures.

Fig. 14. Fracture transmissivity (red circles) and $(1/T_1) \times (dT/dh)$ (blue crosses) estimated by flow simulation with respect to test-section pressure during each injection step. T_1 is baseline transmissivity (m^2 s^{-1}), T is transmissivity (m^2 s^{-1}), and h is hydraulic head (m). (For interpretation of the references to colour in this figure legend, the reader is referred to the Web version of this article.)

Considering that these steps might have been affected by gas (degassed CH$_4$ and CO$_2$)[45] left within the tested fractures, the simulation results for those steps were excluded from the following discussion.

Fig. 14 plots T and $(1/T_1) \times (dT/dh)$ with respect to the test-section pressure, where T_1 for each injection test is the T during step 4 for the first test in H4-1, T during step 3 for the second test in H4-1, and T during step 2 for the first and second tests in H4-3. Both T and $(1/T_1) \times (dT/dh)$ gradually increased with increasing test-section pressure, where T increased from 3 to 4×10^{-8} to 3×10^{-7} m^2 s^{-1} for H4-1 and from 1 to 2 $\times 10^{-8}$ to 2×10^{-7} m^2 s^{-1} for H4-3 (Fig. 14; Tables 2 and 3). The value

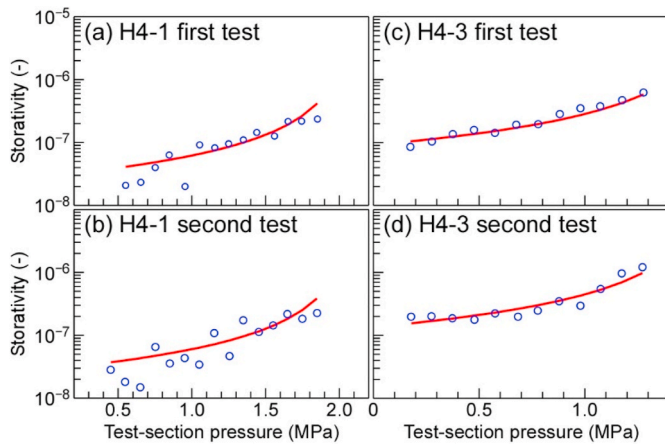Fig. 15. Fracture storativity estimated by flow simulation (blue circles) and from the hydromechanical model (Eq (3), (8), and (13)) (red curves) with respect to test-section pressure during each injection step. (For interpretation of the references to colour in this figure legend, the reader is referred to the Web version of this article.)
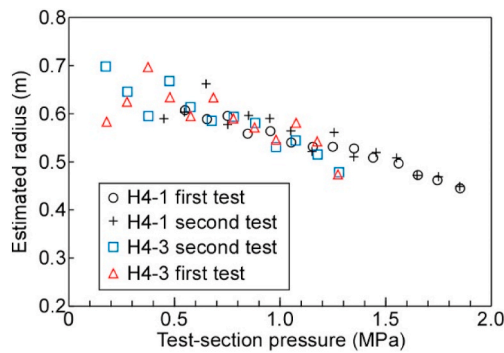

Fig. 16. Radius of the assumed aquifer estimated by flow simulation during each injection step.

of $(1/T_1) \times (dT/dh)$ was of the order of 10^{-2} m^{-1} or less, with H4-1 showing a lower value than H4-3 (Fig. 14; Tables 2 and 3).

The estimated S gradually increased with increasing test-section pressure by a factor of 8–11 for H4-1 and by a factor of 6–7 for H4-3 (blue circles in Fig. 15). The simulated radius was 0.45–0.66 m for H4-1 (Table 2) and 0.47–0.70 m for H4-3 (Table 3), which gradually decreased with increasing test-section pressure (Fig. 16). Another fitting analysis adding the flow dimension as a fitting parameter resulted in flow dimensions of 1.95–2.20 for H4-1 and 1.83–2.32 for H4-3 (Table 4), which are close to 2.0.

Figs. 17 and 18 show the results of the fitting analysis using the hydromechanical model expressed by Eqs (3), (8) and (13). They plot the flow-simulation-based e and the hydromechanical model-based e (fitted curves) with respect to σ'_n. Table 5 lists the estimated σ_n, E_0, and K_{ni}; the best estimations of σ_n were 2.02–2.13 MPa for H4-1 and 1.54–1.61 MPa for H4-3, the former being 0.41–0.59 MPa higher than the latter. The best estimations of E_0 were 0.129–0.214 mm for H4-1 and 0.236–0.454 mm for H4-3. The coefficients of determination were 0.94–1.00 for H4-1 and 0.95–0.99 for H4-3, both of which are very high. The K_{ni} was 2–5 MPa mm^{-1} for H4-1 and 1–3 MPa mm^{-1} for H4-3, following Eqs (6) and (7).

Tables 2 and 3 and Fig. 19 show other parameters E, K_n, α, and σ'_n estimated using Eqs (8) and (12)–(14) and the mean values for JRC_0 and σ_t. With decreasing σ'_n, E increases from 0.04 to 0.07 mm for H4-1 and from 0.08 to 0.13 mm for H4-3, K_n decreases from 62 to 65 to 17–18 MPa mm^{-1} for H4-1 and from 25 to 9–10 MPa mm^{-1} for H4-3, and α

increases from 0.3 to 0.7 for H4-1 and from 0.3 to 0.6–0.7 for H4-3. The range of E was 0.04–0.13 mm, and K_n was of the order of 10 MPa mm^{-1}; H4-1 had a lower K_n than did H4-3, and α was apparently lower than 1.0 (Fig. 19). Fracture storativity calculated from K_n and Eq (15) increased gradually by up to a factor of 10 for H4-1 and by up to a factor of 6 for H4-3 with increasing test-section pressure (red curves in Fig. 15); changes in S were very similar to those estimated by flow simulation (blue circles in Fig. 15).

5. Discussion

5.1. Reliability of the estimated values of σ_n, E_0, and other parameters

The present study applied the Barton-Bandis model involving Eqs (3), (8) and (13) to determine σ_n, E_0, and other parameters by fitting the flow simulation-based e and hydromechanical model-based e during the injection tests. The fitting analysis gave very high coefficients of determination (i.e., 0.94–1.00 for H4-1 and 0.95–0.99 for H4-3; Table 5). Thus, the hydromechanical model appears able to quantify σ_n, E_0, and other parameters. This result is also supported by the following discussion.

(1) The value of σ_n for H4-1 was estimated to be 0.41–0.59 MPa higher than that for H4-3. This means the two boreholes have differing principal stress states, as the tested fractures exhibit similar directions and are located at similar positions against Niche No. 4 (Fig. 2). At the west side of Niche No. 4, the total stress of ~0.2 MPa was widely applied to the shotcrete from inside the tunnel owing to the groundwater (saline water) supply and weak swelling of backfilling materials, as shown in Fig. 6. It is therefore reasonable that the value of σ_n for H4-1 was higher than that for H4-3. Although the applied total stress (~0.2 MPa) is smaller than the difference of σ_n (i.e., 0.41–0.59 MPa), this shortage can be attributed to heterogeneity of stress disturbance caused by tunnel excavation; i.e., more numerous EDZ fractures develop in and around the H4-3 test section compared with that of H4-1 (Fig. 2). Thus, the stress magnitude around the H4-3 test section may be smaller than that of H4-1 because of the greater stress relaxation associated with more intensive EDZ fracturing. As the pressure cells installed on the shotcrete near the test section of H4-1 (TPB018 and TPB019 in Fig. 2a and b) did not measure significant change during injection (Fig. 13), any variation in total stress around the test sections during injection testing was insignificant.

(2) The estimated values of E_0 were 0.129–0.214 mm for H4-1 and 0.236–0.454 mm for H4-3. These values are consistent with other results. Previous hydromechanical characterization of the EDZ and related numerical analysis indicated that the transmissivity of poorly self-sealed EDZ fractures is similar to that of water-conducting fractures in fault zones if they are under the same stress conditions.[30] Other previous work[29] has indicated that the stress dependence of transmissivity along water-conducting fractures in fault zones can be explained by the Barton–Bandis model, and showed that the range of E_0 (from its minimum, E_{0min}, to its maximum, E_{0max}) for such fractures in fault zones can be represented empirically by the following equations:

$$E_{0max} = 0.737 R_z \tag{16}$$

$$E_{0min} = 0.037 R_z. \tag{17}$$

From the R_z values of 0.9–1.1 mm for H4-1 and 2.7–3.9 mm for H4-3 (Fig. 5), these equations give the expected ranges of E_0 as 0.033–0.811 mm for H4-1 and 0.100–2.874 mm for H4-3. The estimated values of E_0 (i.e., 0.129–0.214 mm for H4-1 and 0.236–0.454 mm for H4-3) seem reasonable, as they are within the expected ranges (Fig. 20).

Table 4

Transmissivity T (m^2 s^{-1}), storativity S (–), radius r (m), and flow dimension n (–) estimated by flow simulation during each injection step for H4-1 and H4-3.

Step no.	Flow simulation				Step no.	Flow simulation			
	T	S	r	n		T	S	r	n
H4-1 first test					H4-3 first test				
4	3.66×10^{-8}	1.24×10^{-8}	0.66	2.14	2	2.13×10^{-8}	9.90×10^{-8}	0.67	2.03
5	3.98×10^{-8}	1.41×10^{-8}	0.58	2.05	3	2.42×10^{-8}	1.12×10^{-7}	0.64	1.99
6	3.53×10^{-8}	2.89×10^{-8}	0.44	2.11	4	1.76×10^{-8}	1.33×10^{-7}	0.63	2.27
7	5.20×10^{-8}	1.23×10^{-8}	0.59	1.95	5	2.24×10^{-8}	1.00×10^{-7}	0.68	2.20
8	4.81×10^{-8}	1.37×10^{-8}	0.54	2.06	6	2.57×10^{-8}	1.15×10^{-7}	0.64	2.08
9	4.93×10^{-8}	4.17×10^{-8}	0.29	2.01	7	3.80×10^{-8}	1.03×10^{-7}	0.65	1.83
10	5.30×10^{-8}	4.88×10^{-8}	0.33	1.96	8	2.80×10^{-8}	1.13×10^{-7}	0.57	2.01
11	5.34×10^{-8}	5.75×10^{-8}	0.38	2.01	9	4.15×10^{-8}	1.30×10^{-7}	0.57	1.87
12	5.95×10^{-8}	8.74×10^{-8}	0.31	2.05	10	3.73×10^{-8}	1.05×10^{-7}	0.52	2.00
13	7.14×10^{-8}	1.26×10^{-7}	0.21	2.05	11	5.79×10^{-8}	2.31×10^{-7}	0.48	1.97
14	8.90×10^{-8}	1.60×10^{-7}	0.20	2.04	12	9.91×10^{-8}	4.35×10^{-7}	0.49	1.99
15	1.19×10^{-7}	1.35×10^{-7}	0.15	2.09	13	1.93×10^{-7}	6.14×10^{-7}	0.48	2.10
16	1.71×10^{-7}	1.75×10^{-7}	0.17	2.12					
17	2.97×10^{-7}	1.58×10^{-7}	0.18	2.10					
H4-1 second test					H4-3 second test				
3	3.21×10^{-8}	1.15×10^{-8}	0.61	2.14	2	1.85×10^{-8}	1.84×10^{-7}	0.65	2.10
4	2.89×10^{-8}	7.21×10^{-9}	0.58	2.20	3	2.07×10^{-8}	2.35×10^{-7}	0.64	2.13
5	3.56×10^{-8}	7.51×10^{-9}	0.60	2.07	4	1.93×10^{-8}	2.70×10^{-7}	0.59	2.14
6	2.96×10^{-8}	1.08×10^{-8}	0.56	2.17	5	1.88×10^{-8}	2.74×10^{-7}	0.59	2.24
7	3.39×10^{-8}	9.22×10^{-9}	0.50	2.09	6	2.56×10^{-8}	2.73×10^{-7}	0.63	2.04
8	4.10×10^{-8}	1.47×10^{-8}	0.55	1.95	7	2.66×10^{-8}	2.70×10^{-7}	0.63	2.06
9	4.43×10^{-8}	2.30×10^{-8}	0.55	2.00	8	2.69×10^{-8}	2.79×10^{-7}	0.61	2.12
10	4.22×10^{-8}	9.81×10^{-8}	0.50	2.07	9	3.61×10^{-8}	2.77×10^{-7}	0.57	2.01
11	5.33×10^{-8}	9.82×10^{-8}	0.49	1.98	10	3.79×10^{-8}	2.38×10^{-7}	0.55	2.10
12	5.81×10^{-8}	1.63×10^{-7}	0.50	2.03	11	4.59×10^{-8}	3.89×10^{-7}	0.44	2.32
13	6.96×10^{-8}	1.50×10^{-7}	0.51	2.04	12	1.41×10^{-7}	6.63×10^{-7}	0.51	1.96
14	8.80×10^{-8}	1.58×10^{-7}	0.49	2.06	13	2.05×10^{-7}	9.33×10^{-7}	0.48	2.19
15	1.16×10^{-7}	1.54×10^{-7}	0.48	2.10					
16	1.67×10^{-7}	1.56×10^{-7}	0.46	2.12					
17	2.57×10^{-7}	1.53×10^{-7}	0.45	2.10					

(3) Estimates of other related parameters such as K_n and E also seem reasonable. The estimated K_n was of the order of 10 MPa mm^{-1} (Fig. 19b), which is within the range (1–1000 MPa mm^{-1}) commonly reported by previous field investigations.[49,72–79] The value of S derived from K_n also varied similarly to that derived from flow simulation (Fig. 15). The value of K_n should also be related to $(1/T_1) \times (dT/dh)$, as both parameters indicate the stress dependence of fracture transmissivity[49]; the estimated K_n was higher for H4-1 than for H4-3 (Fig. 19b), consistent with the relation for $(1/T_1) \times (dT/dh)$ observed between H4-1 and H4-3 (Fig. 14; conversely lower for H4-1 than for 4-3). The estimated range of E (0.04–0.13 mm) was also consistent with the range (0.03–0.31 mm) observed in previous resin-injection tests in the study area.[41]

Consider next the radius estimated by flow simulation, which was 0.45–0.70 m (Tables 2 and 3), consistent with (but somewhat larger than) the expected size of the tested fractures based on geological wall-mapping during tunnel excavation (Fig. 3). Therefore, the estimated radius may involve not only the tested single EDZ fractures but also other EDZ fractures linked to the tested fractures. As the estimated radius decreased with increasing test-section pressure (Fig. 16), the following is inferred. Some EDZ fractures were geologically linked to the tested fractures but were not initially linked to them hydraulically (e.g., because of the amount of contact area within the fractures, as indicated by the low α; Fig. 19c); however, the contact area within those fractures gradually reduced with decreasing σ'_n (as indicated from Fig. 19c). The tested fractures thus began to connect hydraulically with other EDZ fractures at locations closer to the test section (injection point), and the effective radius of the assumed aquifer was consequently reduced by the shifting of the constant-head boundary (as shown in Fig. 8b).

5.2. Usability of the method applied here

The method combining constant-head step injection testing and the Barton–Bandis model involving Eqs (3), (8) and (13) appears useful for quantifying/verifying the stress dependence of EDZ's fracture transmissivity, as the fracture e estimated by flow simulation during injection was well reproduced by the model, and the estimated values of σ_n, E_0, and other parameters were also reasonable compared with other observational data or simulation results. The applied method also appears useful in terms of determining the σ_n acting on a fracture. However, the method's applicability might be limited to tensile EDZ fractures in a poorly self-sealed EDZ, as discussed below.

(a) The method requires that fracture-normal displacement occurs before water pressure reaches the σ_n acting on the fracture, as the Barton–Bandis model is applicable when the σ'_n is positive (compressive). This requires the EDZ fracture to be initially permeable. If it is not initially permeable (e.g., due to self-sealing by clay-swelling), fracture-normal displacement may occur when or after water pressure reaches the σ_n acting on the fracture.[80,81] In such cases, theoretical analyses considering only fracture K_n (i. e., Eq (8) or (4)) cannot easily capture the hydromechanical behavior of the fracture, and fully coupled hydromechanical numerical simulations also considering the elasticity of surrounding rock are required.[19,68] Even if fracture-normal displacement occurred before water pressure reaches the σ_n, the water pressure may reach the σ_n during injection. However, such possibility can be assessed by analyzing the coefficient of determination, and the highest coefficient should result when the σ'_n is positive.

(b) Shear-induced dilation may occur during injection.[80] The fractures tested here are tensile EDZ fractures; such fractures tend to be normal to the minimum principal stress. This is supported by
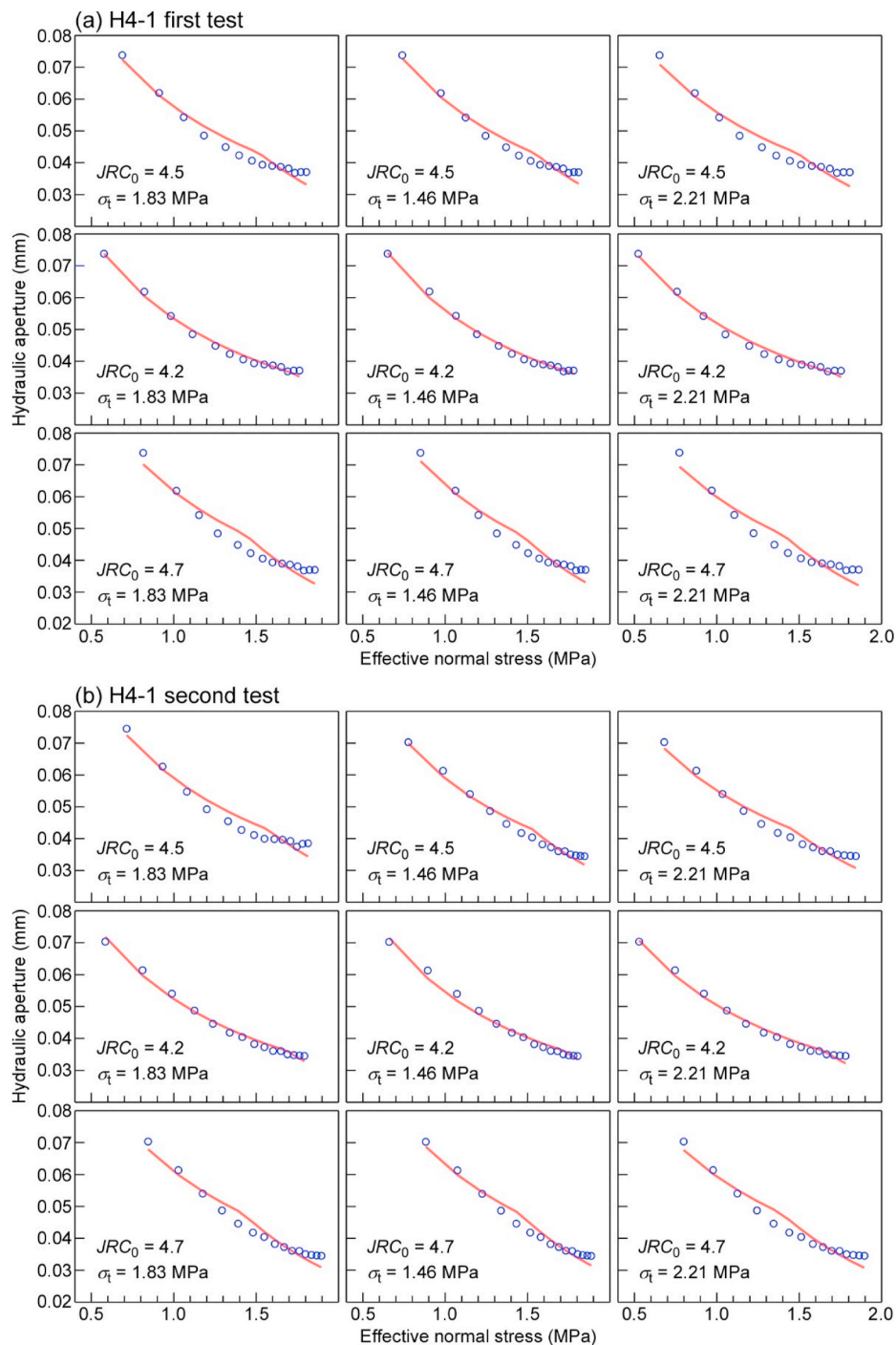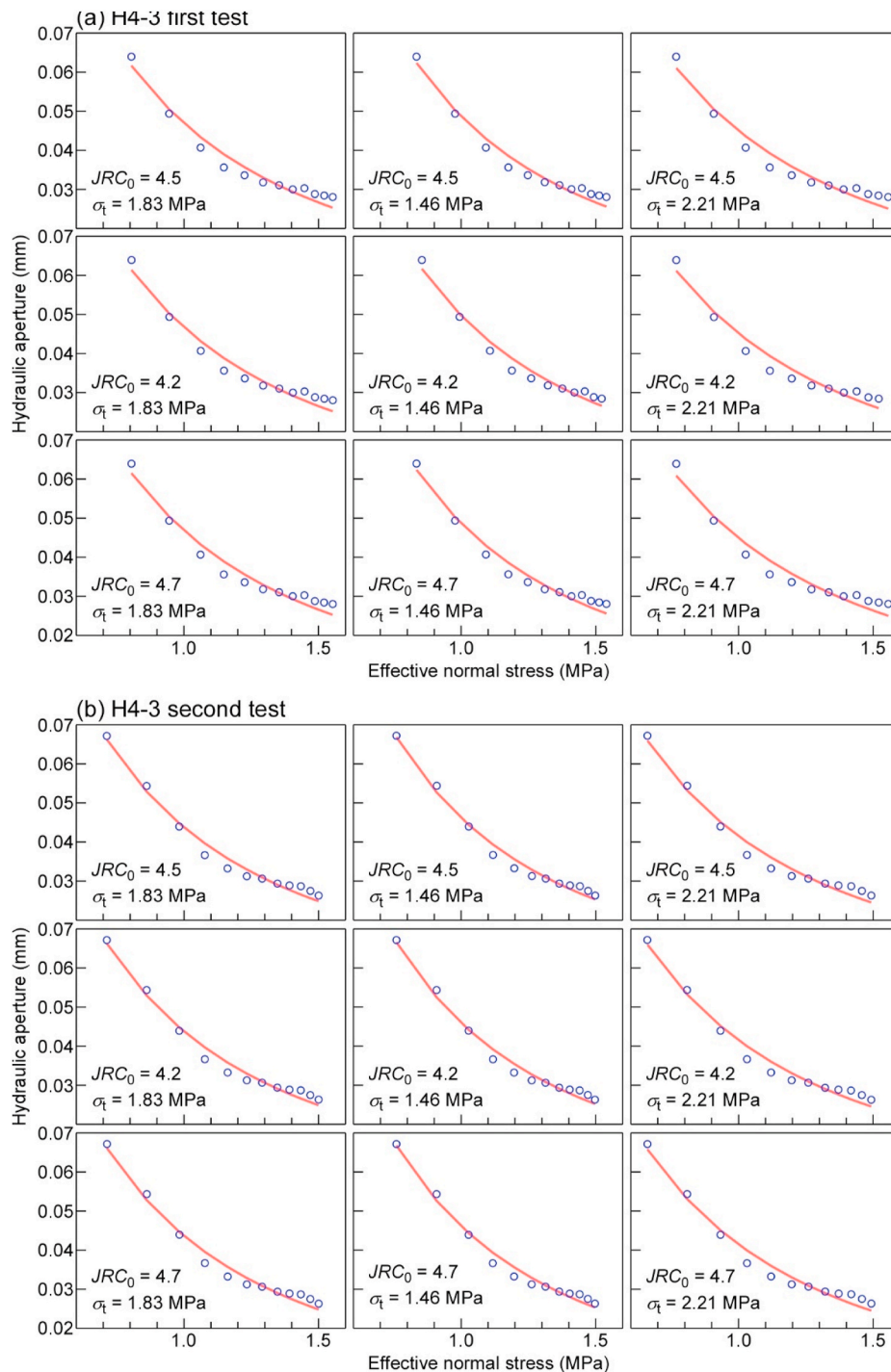
Fig. 17. Results of fitting analysis, showing the relationship between the hydraulic aperture and effective normal stress during the (a) first and (b) second injection tests for H4-1 when given JRC_0 and σ_t which are shown in each figure. JRC_0 is joint roughness coefficient at laboratory scale, and σ_t is indirect tensile strength of intact rock (MPa).

the directions of the fractures being nearly parallel to the wall/-crown of Niche No. 4 (Fig. 2), as the direction of minimum principal stress around a tunnel tends to be normal to the tunnel wall/crown. Therefore, although there is possibility that the EDZ fractures were slightly sheared at/after their formation (i.e., the EDZ fractures are hybrid fractures[82]), shear displacement appears unlikely to have occurred significantly during injection; the high coefficients of determination of the fitting analyses (Table 5) and the reasonable estimates of σ_n, E_0, and other parameters (Section 5.1) indicate that the e during injection was controlled mainly by σ'_n-dependent fracture-normal displacement. However, shear

EDZ fractures[83] might shear during injection testing. Therefore, their analysis might require a model that also considers shear-induced dilation[10,25] and specialized equipment to measure shear displacement precisely during injection.[84–86]

Another problem is the scale effect due to hydrogeological heterogeneity in EDZ fractures. The present study confirmed the flow dimension of the tested EDZ fractures to be close to 2.0 (Table 4). This supported the assumption of homogeneous transmissivity distributions in those fractures, and hence the Barton–Bandis model based on laboratory-scale results could be applied. However, the α estimated by

Fig. 18. Results of fitting analysis, showing the relationship between the hydraulic aperture and effective normal stress during the (a) first and (b) second injection tests for H4-3 when given JRC_0 and σ_t which are shown in each figure. JRC_0 is joint roughness coefficient at laboratory scale, and σ_t is indirect tensile strength of intact rock (MPa).

the hydromechanical model was 0.3–0.7 (Fig. 19c), which is lower than 1.0 and indicates a large amount of contact area within the tested fractures. The estimated radius of the assumed aquifer being dozens of centimeters (Fig. 16) and very small likely led to the flow dimensions of the tested fractures having values close to 2.0, despite the low α. If σ'_n further increases and α further decreases, the flow dimension may no longer be close to 2.0, even within such a limited region around the test section. When the flow dimension reduces to 1.0 or less owing to increased contact area within the fractures, an assumption of homogeneous transmissivity distribution of the EDZ fractures would no longer

hold, as the "effective" transmissivity may decrease with the increasing radius of investigation, even within a limited region. Given this scale effect, the method applied here will predict the minimum reduction in effective transmissivity of EDZ fractures when assuming that σ_n increases by the swelling of backfilling materials; the actual effective transmissivity may be lower than that predicted by the present method.

Table 5

Inputted joint roughness coefficient at laboratory scale JRC_0 (−) and indirect tensile strength of intact rock σ_t (MPa), and estimated normal stress σ_n (MPa), initial mechanical aperture E_0 (mm), coefficients of determination r^2, and initial normal stiffness K_{ni} (MPa mm^{-1}) based on the hydromechanical model (Eq (3), (8), and (13)).

| Input		Simulation result				Input		Simulation result			
JRC_0	σ_t	σ_n	E_0	r^2	K_{ni}	JRC_0	σ_t	σ_n	E_0	r^2	K_{ni}
H4-1 first test						H4-3 first test					
4.5	1.83	2.06	0.166	1.00	3.20	9.3	1.83	1.60	0.321	0.96	1.65
4.5	1.46	2.05	0.200	1.00	2.12	9.3	1.46	1.58	0.381	0.97	1.11
4.5	2.21	2.07	0.143	1.00	4.48	9.3	2.21	1.61	0.279	0.95	2.30
4.2	1.83	2.02	0.154	1.00	3.44	8.4	1.83	1.60	0.282	0.96	1.88
4.2	1.46	2.02	0.188	1.00	2.25	8.4	1.46	1.59	0.339	0.97	0.93
4.2	2.21	2.02	0.133	1.00	4.82	8.4	2.21	1.61	0.246	0.95	2.60
4.7	1.83	2.11	0.178	1.00	2.98	10.7	1.83	1.60	0.382	0.96	1.39
4.7	1.46	2.09	0.214	1.00	1.98	10.7	1.46	1.58	0.454	0.97	1.25
4.7	2.21	2.12	0.153	1.00	4.19	10.7	2.21	1.61	0.332	0.95	1.93
H4-1 second test						H4-3 second test					
4.5	1.83	2.07	0.164	0.97	3.23	9.3	1.83	1.55	0.310	0.98	1.71
4.5	1.46	2.06	0.198	0.97	2.14	9.3	1.46	1.54	0.371	0.99	1.14
4.5	2.21	2.08	0.141	0.96	4.54	9.3	2.21	1.55	0.268	0.98	2.39
4.2	1.83	2.02	0.151	0.99	3.51	8.4	1.83	1.55	0.273	0.98	1.94
4.2	1.46	2.02	0.183	0.99	2.31	8.4	1.46	1.54	0.326	0.99	1.30
4.2	2.21	2.02	0.129	0.99	4.97	8.4	2.21	1.55	0.236	0.98	2.71
4.7	1.83	2.12	0.176	0.95	3.01	10.7	1.83	1.55	0.369	0.98	1.44
4.7	1.46	2.10	0.212	0.97	2.00	10.7	1.46	1.54	0.442	0.99	0.93
4.7	2.21	2.13	0.152	0.94	4.21	10.7	2.21	1.55	0.319	0.98	2.01
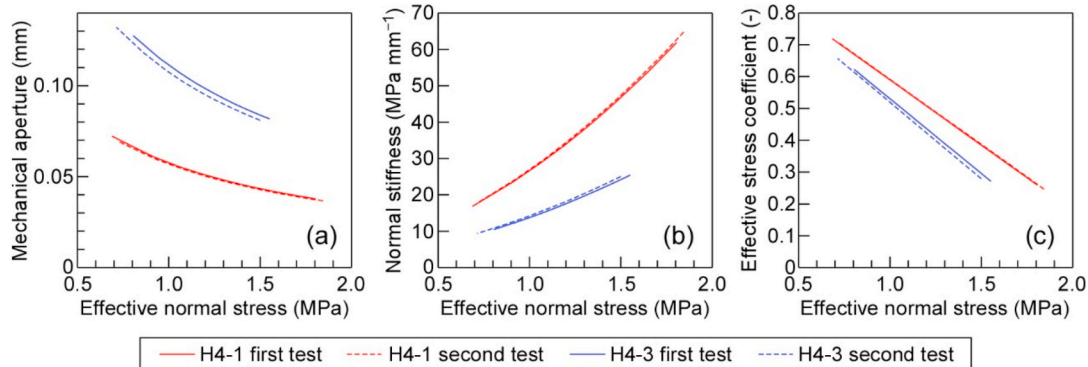
Fig. 19. (a) Fracture mechanical aperture, (b) fracture normal stiffness, and (c) the effective stress coefficient with respect to effective normal stress during the injection tests simulated from the hydromechanical model (Eq (3), (8), and (13)) using the mean values of JRC_0 and σ_t.
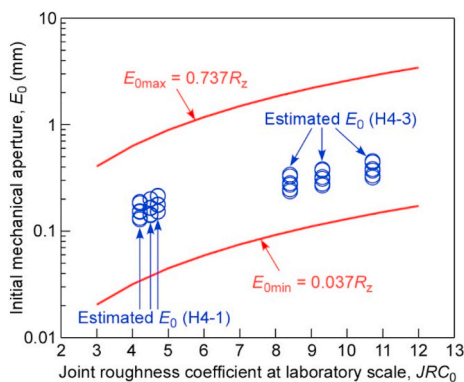

Fig. 20. Initial mechanical aperture estimated by fitting analysis for the injection tests in boreholes H4-1 and H4-3.
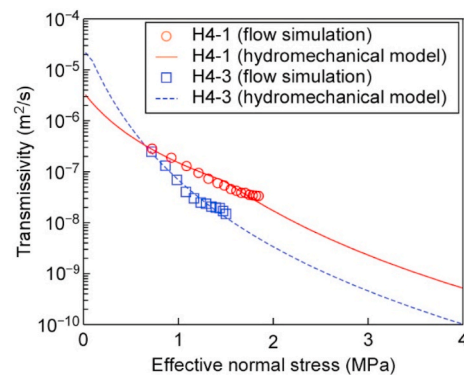

Fig. 21. Change in fracture transmissivity with respect to effective normal stress, estimated by flow simulation and by the hydromechanical model using the results of the second injection tests for H4-1 and H4-3.

5.3. Estimation of the EDZ fracture transmissivity in the post-closure period as a case study

As a case study, the present study simulated the increase in σ'_n required to reduce the transmissivity of the tested EDZ fractures based

on the results of the second injection tests when given the mean values for JRC_0 and σ_t. The two curves in Fig. 21 show the simulation results, where a 2 MPa increase in σ'_n causes fracture transmissivity to reduce by two orders of magnitude, leading to values of T of the order of 10^{-10} m^2 s^{-1} (Fig. 21); i.e., if σ'_n increases by 2 MPa owing to the swelling of

backfilling materials, the transmissivity will become very low. The simulation results in Fig. 21 do not consider the possibility of further reduction of the flow dimension in fractures on a scale of dozens of centimeters; the effective transmissivity may be further reduced when σ'_n further increases above the current σ'_n (i.e., 1.92 MPa for H4-1 and 1.55 MPa for H4-3) and the flow dimension approaches 1.0 or less, as mentioned in Section 5.2.

The present investigation method can promptly evaluate the stress dependence of transmissivity for single EDZ fractures on the scale of dozens of centimeters using measurements from a single borehole. It can also preliminarily evaluate the hydraulic conductivity of the entire EDZ along a tunnel in the post-closure period. However, precise evaluation of an EDZ's hydraulic conductivity requires in situ tunnel-scale experiments and relevant numerical simulations.[18,87] For such large-scale experiments and simulations, the present investigation method can provide reference values of hydromechanical parameters or in situ stress conditions in EDZs.

6. Conclusions

Predicting the permeability of an EDZ during the post-closure period requires quantification of the stress dependence of its fracture transmissivity on the field scale. The present study demonstrates that constant-head step injection tests coupled with the Barton–Bandis σ'_n-dependent fracture-closure model involving Eqs (3), (8) and (13) can potentially quantify/verify the stress dependence of the fracture transmissivity of EDZs at a scale of dozens of centimeters for at least poorly self-sealed, tensile EDZ fractures. The method applied here can also estimate the σ_n acting on the fracture. The injection tests for two single EDZ fractures in the Horonobe URL estimated mechanical parameters. Estimated values of σ_n, E, and K_n during injection were 1.54–2.13 MPa, 0.04–0.13 mm, and 9–65 MPa mm^{-1}, respectively, consistent with other observational data or storativity estimated by flow simulation. Based on the estimated parameters, the transmissivity (of the order of 10^{-8} m^2 s^{-1}) of the tested EDZ fractures was estimated to decrease by at least two orders of magnitude (to 10^{-10} m^2 s^{-1}) when assuming a 2 MPa increase in σ_n due to the swelling of backfilling materials. The proposed investigation method is expected to allow prompt assessment of the stress dependence of EDZs' fracture transmissivity at a given site, and to provide reference values of hydromechanical parameters or in situ stress conditions during precise evaluation of the hydraulic conductivity of the entire EDZ along a tunnel during the post-closure period using in situ tunnel-scale experiments and numerical simulations.

Future works should compare the results of the present study with results from laboratory experiments using core samples containing fractures similar to the tested EDZ fractures and with results from in situ tunnel-scale experiments and numerical simulations.

Declaration of competing interest

The authors declare that they have no known competing financial interests or personal relationships that could have appeared to influence the work reported in this paper.

Data availability

Data are available in Supplementary Material.

Acknowledgements

Appendix A. Supplementary data

Supplementary data to this article can be found online at https://doi.org/10.1016/j.ijrmms.2022.105229.

References

1 OECD/NEA. *International Features, Events and Processes (IFEP) List for the Deep Geological Disposal of Radioactive Waste (Version 3.0)*. Paris, France: OECD/NEA; 2019.
2 Blümling P, Bernier F, Lebon P, Martin CD. The excavation damaged zone in clay formations time-dependent behaviour and influence on performance assessment. *Phys Chem Earth*. 2007;32:588–599.
3 Bock H, Dehandschutter B, Martin CD, et al. *Self-sealing of Fractures in Argillaceous Formations in the Context of Geological Disposal of Radioactive Waste – Review and Synthesis*. Paris: OECD/NEA; 2010. NEA Report 6184.
4 Tsang CF, Barnichon JD, Birkholzer J, Li XL, Liu HH, Sillen X. Coupled thermo-hydro-mechanical processes in the near field of a high-level radioactive waste repository in clay formations. *Int J Rock Mech Min Sci*. 2012;49:31–44.
5 Plúa C, Vu MN, Armand G, et al. A reliable numerical analysis for large-scale modelling of a high-level radioactive waste repository in the Callovo-Oxfordian claystone. *Int J Rock Mech Min Sci*. 2021;140, 104574.
6 Thatcher KE, Bond AE, Norris S. Assessing the hydraulic and mechanical impacts of heat generating radioactive waste at the whole repository scale. *Int J Rock Mech Min Sci*. 2021;138, 104576.
7 Xu H, Rutqvist J, Birkholzer J. A study of thermal pressurization and potential for hydro-fracturing associated with nuclear waste disposal in argillaceous claystone. *Int J Rock Mech Min Sci*. 2020;136, 104536.
8 Thatcher KE, Bond AE, Norris S. Pore pressure response to disposal of heat generating radioactive waste in a low permeability host rock. *Int J Rock Mech Min Sci*. 2020;135, 104456.
9 Lei Q, Loew S. Modelling coseismic displacements of fracture systems in crystalline rock during large earthquakes: implications for the safety of nuclear waste repositories. *Int J Rock Mech Min Sci*. 2021;138, 104590.
10 Kwon S, Min K-B. Fracture transmissivity evolution around the geological repository of nuclear waste caused by the excavation damage zone, thermoshearing and glaciation. *Int J Rock Mech Min Sci*. 2021;137, 104554.
11 Bossart P, Trick R, Meier PM, Mayor J-C. Structural and hydrogeological characterisation of the excavation-disturbed zone in the opalinus clay (Mont Terri project, Switzerland). *Appl Clay Sci*. 2004;26:429–448.
12 Baechler S, Lavanchy JM, Armand G, Cruchaudet M. Characterisation of the hydraulic properties within the EDZ around drifts at level −490m of the Meuse/Haute-Marne URL: a methodology for consistent interpretation of hydraulic tests. *Phys Chem Earth, Parts A/B/C*. 2011;36:1922–1931.
13 de La Vaissière R, Armand G, Talandier J. Gas and water flow in an excavation-induced fracture network around an underground drift: a case study for a radioactive waste repository in clay rock. *J Hydrol*. 2015;521:141–156.
14 Marschall P, Giger S, De La Vaissière R, et al. Hydro-mechanical evolution of the EDZ as transport path for radionuclides and gas: insights from the Mont Terri rock laboratory (Switzerland). *Swiss J Geosci*. 2017;110:173–194.
15 Heitz D, Trick T, Bühler C. *Selfrac (SE) Experiment: Long Term Plate Load Experiment*. Mont Terri Project, TN 2003-51. 2003. Swiss Nat. Hydrol. Geol. Surv).
16 Marschall P, Trick T, Lanyon GW, Delay J, Shao H. Hydro-mechanical evolution of damaged zones around a microtunnel in a claystone formation of the Swiss Jura Mountains. In: *The 42nd US Rock Mechanics Symposium*. American Rock Mechanics Association; 2008.
17 Lisjak A, Tatone BSA, Mahabadi OK, et al. Hybrid finite-discrete element simulation of the EDZ formation and mechanical sealing process around a microtunnel in opalinus clay. *Rock Mech Rock Eng*. 2015;49:1849–1873.
18 Alcolea A, Kuhlmann U, Marschall P, et al. *A Pragmatic Approach to Abstract the Excavation Damaged Zone Around Tunnels of a Geological Radioactive Waste Repository: Application to the HG-A Experiment in Mont Terri*. vol. 443. Geological Society, London, Special Publications; 2017:127–147.
19 Rutqvist J, Stephansson O. A cyclic hydraulic jacking test to determine the in situ stress normal to a fracture. *Int J Rock Mech Min Sci Geomech Abstracts*. 1996;43:695–711.
20 Rutqvist J. Fractured rock stress-permeability relationships from in situ data and effects of temperature and chemical-mechanical couplings. *Geofluids*. 2015;15:48–66.
21 Ishii E. A conventional straddle-sliding-packer system as a borehole extensometer: monitoring shear displacement of a fault during an injection test. *Eng Geol*. 2020;275, 105748.
22 Huang Z, Jiang Z, Zhu S, Wu X, Yang L, Guan Y. Influence of structure and water pressure on the hydraulic conductivity of the rock mass around underground excavations. *Eng Geol*. 2016;202:74–84.
23 Barton N. *Modelling Rock Joint Behaviour from in Situ Block Tests: Implications for Nuclear Waste Repository Design*. ONWI-308. Columbus, Ohio: Office of Nuclear Waste Isolation; 1982.
24 Barton N, Bandis S, Bakhtar K. Strength, deformation and conductivity coupling of rock joints. *Int J Rock Mech Min Sci Geomech Abstracts*. 1985;22:121–140.
25 Zhao Z, Guo T, Li S, Wu W, Yang Q, Chen S. Effects of joint surface roughness and orientational anisotropy on characteristics of excavation damage zone in jointed rocks. *Int J Rock Mech Min Sci*. 2020;128, 104265.

26 Azizmohammadi S, Matthäi SK. Is the permeability of naturally fractured rocks scale dependent? *Water Resour Res*. 2017;53:8041–8063.
27 Hsiung SM, Chowdhury AH, Nataraja MS. Numerical simulation of thermal–mechanical processes observed at the drift-scale heater test at Yucca mountain, Nevada, USA. *Int J Rock Mech Min Sci*. 2005;42:652–666.
28 Rutqvist J, Stephansson O. The role of hydromechanical coupling in fractured rock engineering. *Hydrogeol J*. 2003;11:7–40.
29 Ishii E. The highest potential transmissivities of fractures in fault zones: reference values based on laboratory and in situ hydro-mechanical experimental data. *Eng Geol*. 2021;294, 106369.
30 Aoyagi K, Ishii E. A method for estimating the highest potential hydraulic conductivity in the excavation damaged zone in mudstone. *Rock Mech Rock Eng*. 2019;52:385–401.
31 Mazurek M, Eggenberger U. *Mineralogical Analysis of Core Samples from the Horonobe Area*. RWI Technical Report 05-01. 2005. Nagra.
32 Hiraga N, Ishii E. *Mineral and Chemical Composition of Rock Core and Surface Gas Composition in Horonobe Underground Research Laboratory Project (Phase 1)*. *JAEA Technical Report JAEA-Data/Code 2007-022*. Tokai-mura, Japan: Japan Atomic Energy Agency; 2008.
33 Aoki T, Tani T, Sakai K, Koga Y, Aoyagi K, Ishii E. *Poro-elastic Parameter Acquisition Test Using Siliceous Mudstone (Wakkanai Formation)*. JAEA-Research 2020-002. Tokai-mura: Japan Atomic Energy Agency; 2020.
34 Yamamoto T, Shimo M, Fujiwara Y, et al. *HDB-1 Borehole Investigations in Horonobe Underground Research Center*. JNC TJ1400 2002-010. Tokai-mura: Japan Nuclear Cycle Development Institute; 2002.
35 Ishii E, Sanada H, Funaki H, Sugita Y, Kurikami H. The relationships among brittleness, deformation behavior, and transport properties in mudstones: an example from the Horonobe Underground Research Laboratory, Japan. *J Geophys Res*. 2011;116, B09206.
36 International Society for Rock Mechanics. Suggested methods for determining water content, porosity, density, related properties and swelling and slake-durability index properties: Part 2: suggested methods for determining swelling and slake-durability index properties. *Int J Rock Mech Min Sci Geomech Abstracts*. 1979;16:151–156.
37 Yoshino H, Samata Y, Niunoya S, Ishii E. *Hydraulic Tests for the Excavation Damaged Zone Around the 350m Niches in the Horonobe Underground Research Project*. JAEA-Data/Code 2018-015. Tokai-mura, Japan: Japan Atomic Energy Agency; 2019.
38 Suko T, Takano H, Uchida M, et al. *Research on Validation of the Groundwater Flow Evaluation Methods Based on the Information of Geological Environment in and Around Horonobe Underground Research Area*. JNES-RE-2013-9032. Tokyo: Japan Nuclear Energy Safety Organization; 2014.
39 Aoyagi K, Ishii E, Ishida T. Field observations and failure analysis of an excavation damaged zone in the Horonobe underground research laboratory. *Journal of MMIJ*. 2017;133:25–33.
40 Bossart P, Meier PM, Moeri A, Trick T, Mayor J-C. Geological and hydraulic characterisation of the excavation disturbed zone in the opalinus clay of the Mont Terri rock laboratory. *Eng Geol*. 2002;66:19–38.
41 Aoyagi K, Ishii E, Chen Y, Ishida T. Resin-injection testing and measurement of the shear displacement and aperture of excavation-damaged-zone fractures: a case study of mudstone at the Horonobe Underground Research Laboratory, Japan. *Rock Mech Rock Eng*. 2022;55:1855–1869.
42 Li Y, Zhang Y. Quantitative estimation of joint roughness coefficient using statistical parameters. *Int J Rock Mech Min Sci*. 2015;77:27–35.
43 Nakayama M, Ohno H. *The In-Situ Experiment for Performance Confirmation of Engineered Barrier System at Horonobe Underground Research Laboratory -installation of Engineered Barrier System and Backfilling the Test Niche at the 350m Gallery*. JAEA-Research 2019-007. Tokai-mura: Japan Atomic Energy Agency; 2019.
44 Samata Y, Ishii E. *Hydraulic Tests for the Excavation Damaged Zone Around the 350m Niches in the Horonobe Underground Research Project (II)*, 2019-020. JAEA-Data/Code; 2020.
45 Mochizuki A, Ishii E, Miyakawa K, Sasamoto H. Mudstone redox conditions at the Horonobe underground research laboratory, hokkaido, Japan: effects of drift excavation. *Eng Geol*. 2020;267, 105496.
46 Beauheim RL, Roberts RM, Avis JD. Hydraulic testing of low-permeability Silurian and ordovician strata, Michigan basin, southwestern ontario. *J Hydrol*. 2014;509:163–178.
47 Nuclear Waste Management Program. *nSIGHTS Version 2.41a User Manual*. ERMS# 555653. Carlsbad, New Mexico: Sandia National Laboratories; 2011.
48 Snow DT. Rock fracture spacings, openings, and porosities. *J Soil Mech Found Div*. 1968;94:73–92.
49 Schweisinger T, Svenson EJ, Murdoch LC. Introduction to hydromechanical well tests in fractured rock aquifers. *Ground Water*. 2009;47:69–79.
50 Barker JA. A generalized radial flow model for hydraulic tests in fractured rock. *Water Resour Res*. 1988;24:1796–1804.
51 Witherspoon PA, Amick CJ, Gale JE, Iwai K. Observations of a potential size effect in experimental determination of the hydraulic properties of fractures. *Water Resour Res*. 1979;15:1142–1146.
52 Murdoch LC, Germanovich LN. Analysis of a deformable fracture in permeable material. *Int J Numer Anal Methods GeoMech*. 2006;30:529–561.
53 Olsson R, Barton N. An improved model for hydromechanical coupling during shearing of rock joints. *Int J Rock Mech Min Sci*. 2001;38:317–329.
54 Barton N, de Quadros EF. Joint aperture and roughness in the prediction of flow and groutability of rock joints. *Int J Rock Mech Min Sci*. 1997;34:252.
55 Barton N, Quadros E. Understanding the need for pre-injection from permeability measurements: what is the connection? *J Rock Mech Geotech Eng*. 2019;11:576–597.
56 Barton N. A review of mechanical over-closure and thermal over-closure of rock joints: potential consequences for coupled modelling of nuclear waste disposal and geothermal energy development. *Tunn Undergr Space Technol*. 2020;99, 103379.
57 Liu L, Huang Z, Yao J, et al. Simulating two-phase flow and geomechanical deformation in fractured karst reservoirs based on a coupled hydro-mechanical model. *Int J Rock Mech Min Sci*. 2021;137, 104543.
58 Sun L, Grasselli G, Liu Q, Tang X. Coupled hydro-mechanical analysis for grout penetration in fractured rocks using the finite-discrete element method. *Int J Rock Mech Min Sci*. 2019;124, 104138.
59 Blum P, Mackay R, Riley MS. Stochastic simulations of regional scale advective transport in fractured rock masses using block upscaled hydro-mechanical rock property data. *J Hydrol*. 2009;369:318–325.
60 Lei Q, Latham J-P, Xiang J, Tsang C-F, Lang P, Guo L. Effects of geomechanical changes on the validity of a discrete fracture network representation of a realistic two-dimensional fractured rock. *Int J Rock Mech Min Sci*. 2014;70:507–523.
61 Saeidi O, Stille H, Torabi SR. Numerical and analytical analyses of the effects of different joint and grout properties on the rock mass groutability. *Tunn Undergr Space Technol*. 2013;38:11–25.
62 International Society for Rock Mechanics. Suggested methods for determining tensile strength of rock materials. *Int J Rock Mech Min Sci Geomech Abstracts*. 1978;15:99–103.
63 Bandis SC, Lumsden AC, Barton NR. Fundamentals of rock joint deformation. *Int J Rock Mech Min Sci Geomech Abstracts*. 1983;20:249–268.
64 Bandis SC. *Experimental Studies of Scale Effects on Shear Strength and Deformation of Rock Joints*. Ph.D. thesis. University of Leeds; 1980.
65 Biot MA. General theory of three dimensional consolidation. *J Appl Geophys*. 1941;12:155–164.
66 Scholz CH. *The Mechanics of Earthquakes and Faulting*. second ed. Cambridge: Cambridge University Press; 2002.
67 Lei Q, Gholizadeh Doonechaly N, Tsang C-F. Modelling fluid injection-induced fracture activation, damage growth, seismicity occurrence and connectivity change in naturally fractured rocks. *Int J Rock Mech Min Sci*. 2021;138, 104598.
68 Rutqvist J, Graupner B, Guglielmi Y, et al. An international model comparison study of controlled fault activation experiments in argillaceous claystone at the Mont Terri Laboratory. *Int J Rock Mech Min Sci*. 2020;136, 104505.
69 Zhao Z, Chen S, Chen Y, Yang Q. On the effective stress coefficient of single rough rock fractures. *Int J Rock Mech Min Sci*. 2021;137, 104556.
70 Tuncay K, Corapcioglu MY. Effective stress principle for saturated fractured porous media. *Water Resour Res*. 1995;31:3103–3106.
71 Rutqvist J, Noorishad J, Tsang C-F, Stephansson O. Determination of fracture storativity in hard rocks using high-pressure injection testing. *Water Resour Res*. 1998;34:2551–2560.
72 Burbey TJ, Hisz D, Murdoch LC, Zhang M. Quantifying fractured crystallinerock properties using well tests, earth tides and barometric effects. *J Hydrol*. 2012;414–415:317–328.
73 Cappa F, Guglielmi Y, Rutqvist J, Tsang C-F, Thoraval A. Hydromechanical modelling of pulse tests that measure fluid pressure and fracture normal displacement at the Coaraze Laboratory site, France. *Int J Rock Mech Min Sci*. 2006;43:1062–1082.
74 Guglielmi Y, Elsworth D, Cappa F, et al. In situ observations on the coupling between hydraulic diffusivity and displacements during fault reactivation in shales. *J Geophys Res Solid Earth*. 2015;120:7729–7748.
75 Jeanne P, Guglielmi Y, Rutqvist J, Nussbaum C, Birkholzer J. Permeability variations associated with fault reactivation in a claystone formation investigated by field experiments and numerical simulations. *J Geophys Res Solid Earth*. 2018;123:1694–1710.
76 Murdoch LC, Hisz DB, Ebenhack JF, Fowler DE, Tiedeman CR, Germanovich LN. Analysis of hydromechanical well tests in fractured sedimentary rock at the NAWC Site, New Jersey. In: *Proceedings of the 43rd US Rock Mechanics Symposium and 4th U.S.-Canada Rock Mechanics Symposium, ARMA 09-201*. Asheville: American Rock Mechanics Association; 2009.
77 Schweisinger T, Svenson EJ, Murdoch LC. Hydromechanical behavior during constant-rate pumping tests in fractured gneiss. *Hydrogeol J*. 2011;19:963–980.
78 Svenson E, Schweisinger T, Murdoch LC. Analysis of the hydromechanical behavior of a flat-lying fracture during a slug test. *J Hydrol*. 2007;347:35–47.
79 Svenson E, Schweisinger T, Murdoch LC. Field evaluation of the hydromechanical behavior of flat-lying fractures during slug tests. *J Hydrol*. 2008;359:30–45.

80 Dutler N, Valley B, Gischig V, et al. Hydromechanical insight of fracture opening and closure during in-situ hydraulic fracturing in crystalline rock. *Int J Rock Mech Min Sci*. 2020;135, 104450.

81 Guglielmi Y, Nussbaum C, Jeanne P, Rutqvist J, Cappa F, Birkholzer J. Complexity of fault rupture and fluid leakage in shale: insights from a controlled fault activation experiment. *J Geophys Res Solid Earth*. 2020;125, e2019JB017781.

82 Ishii E. Far-field stress dependency of the failure mode of damage-zone fractures in fault zones: results from laboratory tests and field observations of siliceous mudstone. *J Geophys Res Solid Earth*. 2016;121:70–91.

83 Armand G, Leveau F, Nussbaum C, et al. Geometry and properties of the excavation-induced fractures at the meuse/haute-marne URL drifts. *Rock Mech Rock Eng*. 2014; 47:21–41.

84 Guglielmi Y, Cappa F, Lançon H, et al. ISRM suggested method for step-rate injection method for fracture in-situ properties (SIMFIP): using a 3-components borehole deformation sensor. *Rock Mech Rock Eng*. 2014;47:303–311.

85 Park J-W, Guglielmi Y, Graupner B, et al. Modeling of fluid injection-induced fault reactivation using coupled fluid flow and mechanical interface model. *Int J Rock Mech Min Sci*. 2020;132, 104373.

86 Shiu W, Guglielmi Y, Graupner B, Rutqvist J. Modelling the water injection induced fault slip and its application to in-situ stress estimation. *Int J Rock Mech Min Sci*. 2021;137, 104537.

87 Lanyon GW, Marschall P, Trick T, De La Vaissière R, Shao H, Leung H. *Self-sealing Experiments and Gas Injection Tests in a Backfilled Microtunnel of the Mont Terri URL*. vol. 400. Geological Society, London, Special Publications; 2014:93–106.